

Constitutive modeling of solid propellant materials with evolving microstructural damage

F. Xu^a, N. Aravas^b, P. Sofronis^{a,*}

^a*Department of Mechanical Science and Engineering, University of Illinois at Urbana-Champaign, 1206 West Green Street, Urbana, IL 618011, USA*

^b*Department of Mechanical and Industrial Engineering, University of Thessaly, Pedion Areos, 38334 Volos, Greece*

Received 26 April 2007; received in revised form 25 October 2007; accepted 31 October 2007

Abstract

Solid propellants are composite materials with complex microstructure. In a generic form, the material consists of polymeric binder, crystal oxidizer (e.g., ammonium perchlorate), and fuel particles (e.g., aluminum). Severe stressing and extreme temperatures induce damage which is manifested in particle cracking, dewetting along particle/polymer interfaces, void nucleation and growth. Damage complicates the overall constitutive response of a solid propellant over and above the complexities associated with the differing constitutive properties of the particle and binder phases. Using rigorous homogenization theory for composite materials, we propose a general 3-D nonlinear macroscopic constitutive law that models microstructural damage evolution upon straining through continuous void formation and growth. The law addresses the viscous deformation rate within the framework of additive decomposition of the deformation rate and the concept of back stress is used to improve the model performance in stress relaxation. No restriction is placed on the magnitude of the strains. Experimental data from the standard relaxation and uniaxial tension tests are used to calibrate the model parameters in the case of a high elongation solid propellant. It is emphasized that the model parameters are descriptors of individual phase constitutive response and criticality conditions for particle decohesion which can systematically be determined through experiment. The model is used to predict the response of the material under more complex loading paths and to investigate the effect of crack tip damage on the mechanical behavior of a compact tension fracture specimen.

© 2007 Elsevier Ltd. All rights reserved.

Keywords: Viscoelastic; Homogenization; Constitutive law; Void; Particle dewetting

1. Introduction

The microstructure of a typical solid propellant material consists of polymeric binder, oxidizer, metal fuel, and some other additives for improved bonding and burning (Sutton, 1986; Özüpek and Becker, 1992). From a mechanical behavior perspective, each of these phases exhibits a complex constitutive response that varies with temperature and load.

*Corresponding author. Fax: +1 217 244 6534.

E-mail address: sofronis@uiuc.edu (P. Sofronis).

The binder is a rubbery material, e.g., polybutadiene-acrylonitrile-acrylic acid (PBAN) or hydroxy-terminated polybutadiene (HTPB), that behaves viscoelastically and serves as a cushion for the oxidizer, e.g., ammonium perchlorate, which is an organic crystal with response predominantly elastic in comparison to the elastomeric binder. The fuel, e.g., powdered aluminum, is elastoplastic owing to its metallic nature. The characterization of the overall constitutive response of such a composite material under load poses challenging problems as it requires the coupling of deformation of the constituent phases in entirely different regimes, namely, elastic and viscous. The problem becomes even more complex (Özüpek and Becker, 1992), if one considers the evolution of the microstructure as large oxidizer particles debond from the matrix, a process called *dewetting* (Farris, 1968; Cornwell and Schapery, 1975; Vratsanos and Farris, 1993a, b), during straining and interfacial microcracks or holes are forming as shown schematically in Fig. 1. In fact, this microstructural damage is a sufficient reason for the material to exhibit a strong nonlinear macroscopic response.

For a thorough review of the previous work in the area of propellant constitutive modeling, one may look at the work of Schapery and his co-workers (e.g., Park and Schapery, 1997; Ha and Schapery, 1998) who have investigated the elastic and viscoelastic response of damaged composite propellant materials over the last 25 years. Briefly reviewing their most recent work, one may refer to the constitutive theory for elastic media with damage (Schapery, 1990) and to the potential theory approach to modeling the effect of damage on the elastic constitutive response of particle-filled rubber on the basis of an internal damage parameter (Schapery, 1991). Later, Park and Schapery (1997) addressed the effect of time-dependent damage (e.g., microcracking) on the viscoelastic axisymmetric response of a solid propellant through two state variables corresponding to the dissipated work associated with the elastic and viscous character of the propellant, respectively. Ha and Schapery (1998) modified the model of Park and Schapery to address three-dimensional (3-D) stress states. While the theoretical predictions agree with the experimental results on the ascending part of the load–displacement response, they fail to address the descending part of the curve. Hinterhoelzl and Schapery (2004) modified the model of Ha and Schapery (1998) to account for the evolution of the material from the undamaged, compressible, and isotropic state before deformation to one with damage-induced anisotropy upon straining in a small-strain framework. In addition, they modified the parameters involved in the constitutive relationship between stresses and pseudo-strains to improve convergence in the finite element implementation of the model.

Characterization of the constitutive response of solid propellant materials in the presence of damage has been the objective of several other investigations in the past 30 years. The model of Simo (1987) is a rigorous 3-D finite-strain approach to the study of damage in a viscoelastic medium from a continuum mechanics viewpoint. Swanson and Christensen (1983) presented a constitutive model in which a strain softening function was used to describe the viscoelastic response of a high elongation solid propellant expressed in the form of a hereditary integral. Francis and Thompson (1984) used the same softening function approach as Swanson and Christensen (1983) in order to address complex loading and unloading situations, but their constitutive model requires a large number (four) of calibration experiments. Özüpek and Becker (1992) combined these two models to simulate finite-strain uniaxial response of a high elongation polyethyleneglycol/nitroglycerin (PEG/NG) solid

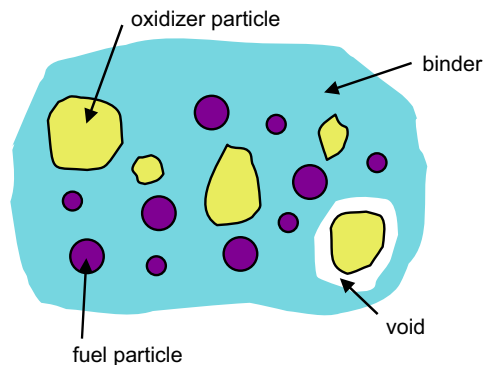


Fig. 1. Schematic of a solid propellant microstructure. Voids can form by dewetting at oxidizer particles.

propellant. The model employs a softening function, determined experimentally, to account for the effect of damage on the deviatoric response of the propellant and requires assumptions on the material compressibility. Following the damage approach of Schapery (1981, 1989), Gazonas (1993) proposed a one-dimensional (1-D) nonlinear viscoelastic constitutive model to describe the mechanical behavior of a solid propellant in the presence of microcrack growth. To address the issue of volume dilatation upon straining, the effect of superposed pressure, and the cyclic response of propellants in multiaxial stressing for the Space Shuttle redesigned solid rocket motor, Özüpek and Becker (1997) introduced a new version of their constitutive viscoelastic model based on phenomenological descriptions of dilatation and free energy functions to account for damage. A calibration of a number of parameters is required prior to using the model for numerical simulation predictions. A modification of this model in order to be used in finite element simulations was done by Canga et al. (2001). These researchers considered that the presence of voids affected the volumetric response by reducing the bulk modulus, softened the deviatoric response which was described by means of a damage function, and affected the dissipation work on cyclic loading through another cyclic loading function. A constitutive model based on the work of Simo (1987) and similar to that of Özüpek and Becker (1992, 1997) was introduced by Jung and Youn (1999). This model accounts for dewetting by allowing for a decrease in the viscoelastic modulus due to dewetting. Jung et al. (2000) extended this model by modifying the damage function parameters in order to better describe cyclic loading. In the last two models, the critical condition for dewetting and hence the calculation of the related modulus softening response is based on the work of Farber and Farris (1987) and Vratsanos and Farris (1993a, b) which addresses dewetting in pure elastic media and without considering the complex deformation fields upon dewetting.

Studying the response of solid propellants (e.g., HTPB/ammonium perchlorate) under high strain-rates ranging between 10^3 and 10^4 s^{-1} , Ho (2002) used a softening pre-multiplier to describe 1-D nonlinear viscoelastic response. He assumed that this parameter was a function of strain rate and recoverable deformation energy which he determined from loading/unloading data in uniaxial tension. Ho claims that his recoverable energy approach is better than the Swanson and Christensen (1983) and Francis and Thompson (1984) approaches in which damage was introduced in the constitutive law as a function of stress. Based on extensive experiments, Matheson and Nguyen (2005) developed a viscoelastic damage model to simulate the nonlinear behavior of a solid propellant material under different loading conditions. The model is basically a Maxwell-type one in which the constitutive parameters are treated as functions of time and damage. The model predicts successfully tensile response under both high and low strain rates and quite well the Taylor test. A constitutive law for the small-strain response of a porous viscoelastic solid under 3-D triaxial stress states has been proposed recently by Xu et al. (2007). The model was calibrated through the shear relaxation test and used to predict the response of a solid propellant whose damage during straining was simulated by the presence of changing porosity. For the behavior under cycling loading, the model reproduces the loading response observed in the experiments of Özüpek and Becker (1997), but it does not capture the nonlinear features of the response upon unloading.

Matouš and Geubelle (2006) studied particle dewetting at a unit cell comprising of one or four hyperelastic particles embedded in a hyperelastic particle-reinforced matrix whose constitutive behavior was found by the Mori–Tanaka homogenization scheme. The particle–matrix interface was described by a cohesive law. The simulations indicated that even after complete debonding the presence of the particles continue to impart stiffness in the material. Tan et al. (2005a) devised an experimental method to analyze a compact tension specimen and extract the microscale cohesive law for the particle/matrix interface of high explosive PBX9501 by using the extended Mori–Tanaka method (Mori and Tanaka, 1973) to homogenize the composite material response. The cohesive law was then used to study the effect of interfacial debonding on the mechanical behavior of particulate composites under hydrostatic tension and uniaxial tension conditions (Tan et al., 2005b, 2007). The results show that small particles tend to stiffen the composite whereas large particles cause softening. The research also identified a critical particle radius that separates these two regimes of behavior.

An interesting piece of work that couples experimental measurements with a modeling approach that accounts for the underlying phenomenological mechanisms of deformation and material constitution is the work by Trumel et al. (2001a, b). Investigating the response of a solid propellant in compression under various paths of static and dynamic loading, Trumel et al. (2001a) found that particle dewetting and crushed grains is

the prevalent mode of damage which reduces the macroscopic stiffness of the material in both tension and compression tests. Trumel et al. (2001a, b) developed a viscoelastoplastic compaction model to characterize both static and dynamic response through a thermodynamic potential function. A scalar function of the first invariant of the viscoplastic strain was used to describe the compaction and damage-related dilatancy due to particle–matrix debonding (Trumel et al., 1996, 2001a, b). Compared with static and dynamic experimental data from 1-D and 2-D cases, the model yielded satisfactory predictions and captured important aspects of the material behavior such as rate-dependence, hardening and softening, and dilatation. In the case of a simulation of dynamic penetration of the material, the model predicted a maximum temperature increase by 40 °C due to the inelastic energy dissipation. However, Ravichandran and Liu (1995) point out that this treatment via a thermodynamic potential might underestimate the dependence of bulk modulus on particle–matrix debonding.

Lastly, we would like to mention the statistical crack mechanics (SCRAM) model of Dienes et al. (2006) which describes the dynamic response and local heating due to friction at crack surfaces of energetic materials, such as explosives and solid propellants. In this model, damage is described by the formation of penny-shaped cracks and the analytical solution for the deformation fields of these cracks is used to describe the damage component of the total deformation rate tensor. Issues such as crack orientation, growth and coalescence, and nonlinear elastoplastic behavior of the matrix material are accounted for. The model predictions in uniaxial tension are in good agreement with the experiment. The model was also used to predict hot spot generation in high explosives under dynamic impact.

The discussion above indicates that the majority of the existing models are based on a number of phenomenological constants and functions of deformation characteristics to describe the effect of damage separately on the deviatoric and volumetric response of a propellant. Use of the models requires in some cases calibration of these parameters and interestingly enough, some models introduced for uniaxial tension require that they be modified when applied to multiaxial stress situations. Further, some models fail to reproduce the material response when massive damage accumulation leads to severe drop in the macroscopic loads (stresses). The objective of this work is to study the response of a solid propellant as affected by damage by using a rigorous solid mechanics methodology. The goal is to suggest a general 3-D constitutive model with physically justified and easy to determine fitting parameters and capable of accounting for the evolution of the microstructure with straining. The development of the model is based on some recent advances of rigorous homogenization theory for nonlinear viscous composites (Ponte Castañeda, 1991; Suquet, 1995, 1996a, b, 1997).

Standard notation is used throughout. Boldface symbols denote tensors the order of which is indicated by the context. All tensor components are written with respect to a fixed Cartesian co-ordinate system, and the summation convention is used for repeated Latin indices. A superscript T indicates the transpose of a second-order tensor, a superposed dot the material time derivative, and the subscripts s and a the symmetric and anti-symmetric parts of a second-order tensor. Let \mathbf{A} , \mathbf{B} be second-order tensors, and \mathbf{C} a fourth-order tensor; the following products are used in the text $\mathbf{A}:\mathbf{B} = A_{ij}B_{ij}$, $(\mathbf{A} \cdot \mathbf{B})_{ij} = A_{ik}B_{kj}$, $(\mathbf{A}\mathbf{B})_{ij} = A_{ij}B_{kl}$, $(\mathbf{C}:\mathbf{A})_{ij} = C_{ijkl}A_{kl}$, and $(\mathbf{A}:\mathbf{C})_{ij} = A_{kl}C_{kl ij}$. The inverse \mathbf{C}^{-1} of a fourth-order tensor that has the “minor” symmetries $C_{ijkl} = C_{jikl} = C_{ijlk}$ is defined so that $\mathbf{C}:\mathbf{C}^{-1} = \mathbf{C}^{-1}:\mathbf{C} = \mathbf{I}$, where \mathbf{I} is the symmetric fourth-order identity tensor with Cartesian components $I_{ijkl} = (1/2)(\delta_{ik}\delta_{jl} + \delta_{il}\delta_{jk})$, δ_{ij} being the Kronecker delta.

2. Constitutive modeling

A solid propellant is a composite material with evolving volume fractions of the individual phases. As described in the introduction, a solid propellant consists of a polymeric matrix, oxidizer particles, metal fuel particles, and some other additives for improved bonding and burning (schematic in Fig. 1). From a mechanical behavior perspective, each of these phases exhibits a complex constitutive response. The binder is a rubbery material that behaves viscously, the oxidizer is predominantly elastic in comparison to the elastomeric binder, and the fuel particles are elastoplastic. Upon straining, large oxidizer particles debond from the matrix and interfacial microcracks or holes are forming as shown schematically in Fig. 1.

We will assume that once dewetting at an oxidizer/matrix interface commences a void forms in the place of the debonded oxidizer particle. Thus, the debonded particle will be treated as a hole in the propellant. For the

case of “pop-loose” decohesion, the replacement of an oxidizer particle by a void is not an unrealistic assumption as dewetting takes place over almost the entire interface. Of course, the presence of the oxidizer particle inside the void does restrain the subsequent growth of the void, but we will assume in our model that the void is capable of growing as if no oxidizer particle were present. Thus, from the constitutive modeling point of view, the material is essentially a three-phase composite that consists of (i) the polymeric binder matrix, (ii) the particles (fuel and oxidizer), and (iii) the voids. For the purposes of modeling, the matrix is assumed to be incompressible linear-elastic viscoplastic, and the particles rigid. Although we do not distinguish between oxidizer and fuel particles, we assume that voids nucleate only at oxidizer particles whose volume fraction is smaller than the total volume fraction of particles. Once nucleated, the voids can grow or close in accordance with the viscous deformation of the surrounding material.

We consider a “representative volume element” (RVE) of the composite with total volume V , and let (V_m, V_p, V_v) denote the volumes of the matrix, particles, and voids in the RVE so that $V = V_m + V_p + V_v$. The volume fractions of the matrix, particles, and voids are, respectively,

$$c_m = \frac{V_m}{V}, \quad c_p = \rho = \frac{V_p}{V}, \quad c_v = f = \frac{V_v}{V}, \quad (1)$$

so that $f + \rho + c_m = 1$. We also define the volume fraction of the particles relative to the matrix as

$$\rho' = \frac{V_p}{V_m + V_p} = \frac{\rho}{1 - f}. \quad (2)$$

The parameter ρ' denotes the volume fraction of particles in the particle-reinforced binder.

The total deformation rate in the composite is written as the sum of an elastic and a viscous part:

$$\mathbf{D} = \mathbf{D}^e + \mathbf{D}^v. \quad (3)$$

The additive split of Eq. (3) is based on the assumption that the elastic and viscous parts can be treated independently and its mechanical analog is the well-known Maxwell model of a spring and a dashpot in series. It must be emphasized though that this is, in general, only an approximation for composite materials. For example, [Suquet \(1985\)](#) demonstrated rigorously that the macroscopic deformation rate of a composite made of nonlinear Maxwell-type phases has a “long memory” term, i.e., the deformation rate of the homogenized medium cannot be written in the form of Eq. (3), even though the response of the individual phases is consistent with Eq. (3). In fact, as we discuss in Section 2.4, we believe that this is one of the reasons that a “back stress” is required to improve the predictions of our model, which is based on the Maxwell-type additive split of Eq. (3).

In the following we discuss in detail the constitutive equations for the individual parts of \mathbf{D} , and the evolution equations of the volume fractions c_m, ρ, f of the phases as the microstructure evolves upon straining.

2.1. Elastic constitutive relations

The elastic response of the incompressible matrix phase is described by a hypoelastic equation of the form

$$\mathbf{D}_m^e = \mathbf{M}_m^e : \overset{\nabla}{\boldsymbol{\sigma}}, \quad \mathbf{M}_m^e = \frac{1}{2\mu_m} \mathbf{K}, \quad \mathbf{J} = \frac{1}{3} \boldsymbol{\delta} \boldsymbol{\delta}, \quad \mathbf{K} = \mathbf{I} - \mathbf{J}, \quad (4)$$

where $\boldsymbol{\sigma}$ is the true (Cauchy) stress tensor, $\overset{\nabla}{\boldsymbol{\sigma}} = \dot{\boldsymbol{\sigma}} + \boldsymbol{\sigma} \cdot \mathbf{W} - \mathbf{W} \cdot \boldsymbol{\sigma}$ is Jaumann or co-rotational derivative, \mathbf{W} the spin tensor, μ_m the elastic shear modulus of the matrix, $\boldsymbol{\delta}$ and \mathbf{I} are the second- and symmetric fourth-order identity tensors, with Cartesian components δ_{ij} (the Kronecker delta) and $I_{ijkl} = (1/2)(\delta_{ik}\delta_{jl} + \delta_{il}\delta_{jk})$.

The elastic homogenization process is carried out in two successive steps ([Bonnafant et al., 1998](#)):

- (i) effective behavior of the matrix containing rigid particles;
- (ii) effective behavior of the homogenized particle-reinforced matrix in (i) above containing voids.

Step I: The [Hashin–Shtrikman \(1963\)](#) lower bound is known to provide an accurate estimate for two-phase composites with the most compliant material occupying the matrix phase. When phase “1” is designated as the

compliant phase, the corresponding estimates take the form

$$\mu_{\text{hom}} = \frac{\sum_{i=1}^2 (c_i \mu_i) / (6\mu_i(\kappa_1 + 2\mu_1) + \mu_1(9\kappa_1 + 8\mu_1))}{\sum_{j=1}^2 (c_j) / (6\mu_j(\kappa_1 + 2\mu_1) + \mu_1(9\kappa_1 + 8\mu_1))}, \quad \kappa_{\text{hom}} = \frac{\sum_{i=1}^2 (c_i \kappa_i) / (3\kappa_i + 4\mu_1)}{\sum_{j=1}^2 c_j / (3\kappa_j + 4\mu_1)}, \quad (5)$$

where $(\mu_{\text{hom}}, \kappa_{\text{hom}})$ are the shear and bulk moduli of the homogenized material, c_i the volume fractions, and (μ_i, κ_i) the shear and bulk moduli of the phases. In our case, $\mu_1 = \mu_m$, $\kappa_1 = \kappa_2 = \mu_2 = \infty$, $c_1 = 1 - \rho' = (1 - f - \rho)/(1 - f)$, and $c_2 = \rho' = \rho/(1 - f)$, so that

$$\mu_{\text{hom}} = \frac{2 - 2f + 3\rho}{2(1 - f - \rho)} \mu_m, \quad \kappa_{\text{hom}} = \infty. \quad (6)$$

Step II: The Hashin–Shtrikman (1963) upper bound is known to provide an accurate estimate for two-phase composites with the stiffest material occupying the matrix phase. When phase “2” is the stiffest one, the corresponding estimates take the form

$$\bar{\mu} = \frac{\sum_{i=1}^2 c_i \mu_i / (6\mu_i(\kappa_2 + 2\mu_2) + \mu_2(9\kappa_2 + 8\mu_2))}{\sum_{j=1}^2 c_j / (6\mu_j(\kappa_2 + 2\mu_2) + \mu_2(9\kappa_2 + 8\mu_2))}, \quad \bar{\kappa} = \frac{\sum_{i=1}^2 c_i \kappa_i / (3\kappa_i + 4\mu_2)}{\sum_{j=1}^2 c_j / (3\kappa_j + 4\mu_2)}, \quad (7)$$

where $(\bar{\mu}, \bar{\kappa})$ are the shear and bulk moduli of the homogenized material. In our case, phase “1” is the voids, and phase “2” is the homogenized particle-reinforced matrix in Step I, so that $\mu_1 = \kappa_1 = 0$, $\mu_2 = \mu_{\text{hom}}$, $\kappa_2 = \kappa_{\text{hom}} = \infty$, $c_1 = f$, and $c_2 = 1 - f$. Then, Eq. (7) imply that

$$\bar{\kappa} = a\mu_m, \quad \bar{\mu} = b\mu_m \quad (8)$$

with

$$a = \frac{2(1 - f)(2 - 2f + 3\rho)}{3f(1 - f - \rho)}, \quad b = \frac{9f}{4(3 + 2f)} a. \quad (9)$$

The elastic part of the constitutive law for the three-phase composite is of the form

$$\mathbf{D}^e = \mathbf{M}^e : \overset{\nabla}{\boldsymbol{\sigma}}, \quad \mathbf{M}^e = \frac{1}{2\bar{\mu}} \mathbf{K} + \frac{1}{3\bar{\kappa}} \mathbf{J}. \quad (10)$$

It should be noted that the *hypoelastic* form (10) is consistent, to leading order, with *hyperelastic* behavior because the elastic strains are small relative to the plastic strains (Needleman, 1985). Note that, even though the matrix material is incompressible ($\kappa_2 = \kappa_{\text{hom}} = \infty$), due to the presence of the voids, the homogenized continuum is compressible, i.e., $\bar{\kappa}$ takes a finite value.

2.2. Viscous constitutive equations

In order to determine the viscous response of the solid propellant material, we use a homogenization technique for nonlinear composite materials introduced by Ponte Castañeda (1991, 1992, 1996).

We proceed with a brief description of the variational procedure. Consider a representative volume element (RVE) V of the composite material, where the size of the inhomogeneities is small compared to that of V . The composite is made up of N homogenous phases $V^{(r)}$, $r = 1, \dots, N$ with volume fractions $c^{(r)}$. The mechanical behavior of each phase “ r ” is described by a viscous potential of the form $\psi^{(r)} = \psi^{(r)}(\sigma_e)$, so that

$$\mathbf{D}^{v(r)} = \frac{\partial \psi^{(r)}}{\partial \boldsymbol{\sigma}} = \overset{\nabla}{\boldsymbol{\varepsilon}}^{v(r)} \quad \mathbf{N} = \frac{1}{2} \theta^{(r)} \mathbf{s} \quad (11)$$

with

$$\mathbf{N} = \frac{3}{2\sigma_e} \mathbf{s}, \quad \overset{\nabla}{\boldsymbol{\varepsilon}}^{v(r)} = \frac{\partial \psi^{(r)}}{\partial \sigma_e}, \quad \theta^{(r)} = \frac{1}{\mu^{(r)}} = \frac{3\overset{\nabla}{\boldsymbol{\varepsilon}}^{v(r)}}{\sigma_e} = \frac{3}{\sigma_e} \frac{\partial \psi^{(r)}}{\partial \sigma_e}, \quad (12)$$

where $\mathbf{D}^{v(r)}$ is the viscous part of the deformation rate of phase r , \mathbf{s} the deviatoric part of the stress tensor $\boldsymbol{\sigma}$, $\theta^{(r)} = 1/\mu^{(r)}$ the viscous shear compliance that depends on the von Mises equivalent stress $\sigma_e = \sqrt{(3/2)\mathbf{s} : \mathbf{s}}$, $\mu^{(r)}$ is the viscous shear modulus, and $\overset{\nabla}{\boldsymbol{\varepsilon}}^{v(r)}$ the equivalent viscous strain.

For a given stress state $\boldsymbol{\sigma}$, the variational procedure involves three steps (deBotton and Ponte Castañeda, 1993; Suquet, 1995, 1996a, b):

1. A linear theory providing an expression for $\mathbf{M}^{\text{hom}}(\theta) = (1/3\bar{\kappa}(\theta))\mathbf{J} + (1/2\bar{\mu}(\theta))\mathbf{K}$ and its partial derivatives with respect to $\theta^{(r)}$, where θ is the collection $\theta = (\theta^{(1)}, \dots, \theta^{(N)})$ and $\theta^{(r)} = 1/\mu^{(r)}$.¹ The compliance tensor $\mathbf{M}^{\text{hom}}(\theta)$ defined above corresponds to a linear composite with given phase compliances $\theta = (\theta^{(1)}, \dots, \theta^{(N)})$.
2. The resolution of $2N$ nonlinear problems for the $2N$ unknowns $(\theta^{(r)}, \sigma_e^{(r)})$:

$$\theta^{(r)} = \frac{3}{\sigma_e^{(r)}} \frac{\partial \psi^{(r)}(\sigma_{eq}^{(r)})}{\partial \sigma_e^{(r)}}, \quad \sigma_e^{(r)} = \sqrt{\frac{3}{c^{(r)}} \boldsymbol{\sigma} : \frac{\partial \mathbf{M}^{\text{hom}}(\theta)}{\partial \theta^{(r)}} : \boldsymbol{\sigma}}. \quad (13)$$

3. Once the $2N$ nonlinear problems (13) are solved and $(\theta^{(r)}, \sigma_e^{(r)})$ are found, $\mathbf{M}^{\text{hom}}(\theta)$ is evaluated and the overall deformation rate is finally given by

$$\mathbf{D}^v = \mathbf{M}^{\text{hom}}(\theta) : \boldsymbol{\sigma} = \frac{p}{3\bar{\kappa}(\theta)} \boldsymbol{\delta} + \frac{1}{2\bar{\mu}(\theta)} \mathbf{s}, \quad (14)$$

where $p = \sigma_{kk}/3$ is the hydrostatic stress. It should be noted that if all N phases are incompressible, then $\bar{\kappa} = \infty$ and $\mathbf{M}^{\text{hom}}(\theta) = (1/2\bar{\mu}(\theta))\mathbf{K}$; however, if one of the phases corresponds to “void” space, then $\bar{\kappa}$ is finite and the composite is compressible.

Suquet (1995, 1996a, b) made the observation that the term on the right-hand side of Eq. (13b) could be identified with the *second* moment of the stress field in the so-called “linear comparison composite.” This provided a new interpretation of the variational method of Ponte Castañeda in terms of a modification of the earlier “secant method,” which made use of the *first* moment of the stress field in the above-mentioned linear comparison composite (Ponte Castañeda and Suquet, 1998).

In our three-phase composite material the values of $\bar{\mu}(\theta)$ and $\bar{\kappa}(\theta)$ to be used in Eq. (14) are given by Eqs. (8) and (9) derived for the corresponding linear material in Section 2.1.

The viscous shear moduli to be used in Eqs. (8) and (9) for the rigid (particles) and void phases take the values ∞ and 0, respectively, and one needs to determine only the proper value of μ_m to be used in Eqs. (8) and (9). This value of μ_m is determined from Eq. (13) as follows: Substitution of Eqs. (8) and (9) in Eq. (14) yields

$$\mathbf{D}^v = \frac{1}{\mu_m} \left(\frac{p}{3a} \boldsymbol{\delta} + \frac{1}{2b} \mathbf{s} \right). \quad (15)$$

Equation (13) takes now the form

$$\sigma_e^{(m)} = \sqrt{\frac{3}{1-\rho-f} \left(\frac{p^2}{a} + \frac{\sigma_e^{(m)2}}{3b} \right)}, \quad \frac{1}{\mu_m} = \frac{3}{\sigma_e^{(m)}} \frac{\partial \psi_m(\sigma_e^{(m)})}{\partial \sigma_e^{(m)}}, \quad (16)$$

where a superscript or a subscript m refers to the matrix material. When the viscous potential Ψ_m for the matrix material is known, Eqs. (14) and (16) define the viscous deformation rate \mathbf{D}^v for a given stress state $\boldsymbol{\sigma}$.

For our problem, we choose for the matrix $\Psi_m(\boldsymbol{\sigma})$ so that

$$\dot{\varepsilon}_m = \frac{\partial \psi_m}{\partial \sigma_e} = \dot{\varepsilon}_0 \left(A \frac{\sigma_e^{(m)}}{\sigma_0} + B \frac{\sigma_e^{(m)2}}{\sigma_0^2} \right)^p (\varepsilon_m)^{-q}, \quad (17)$$

where A , B , p , and q are material constants, and $\varepsilon_m = \int_0^t \dot{\varepsilon}_m dt$, t being time. The special case in which the strain rate $\dot{\varepsilon}_m$ in Eq. (17) is independent of the accumulated viscous strain ε_m (i.e., $q = 0$) corresponds to what is known as “stationary” creep. Note that at a given state of the material the homogenization procedure relates

¹If all N phases are incompressible, then $\bar{\kappa} = \infty$ and $\mathbf{M}^{\text{hom}}(\theta) = (1/2\bar{\mu}(\theta))\mathbf{K}$; however, if one of the phases corresponds to “void” space, then $\bar{\kappa}$ is finite and the composite is compressible.

\mathbf{D}^v to the current stress $\boldsymbol{\sigma}$; the equivalent viscous strain in the matrix ε_m enters the homogenization procedure as a parameter that defines the hardening/softening state of the material.

Summarizing, we note that the constitutive equation for \mathbf{D}^v can be written as

$$\mathbf{D}^v = \frac{1}{3} \dot{\varepsilon}_v \boldsymbol{\delta} + \dot{\varepsilon}_e \mathbf{N}, \quad \mathbf{N} = \frac{3}{2\sigma_e} \mathbf{s}, \tag{18}$$

where

$$\dot{\varepsilon}_v = \frac{p}{a\mu_m}, \quad \dot{\varepsilon}_e = \frac{\sigma_e}{3b\mu_m}, \quad a = \frac{2(1-f)(2-2f+3\rho)}{3f(1-f-\rho)}, \quad b = \frac{9f}{4(3+2f)}a, \tag{19}$$

$$\mu_m = \frac{\sigma_e^{(m)}}{3\dot{\varepsilon}_m}, \quad \sigma_e^{(m)} = \sqrt{\frac{3}{1-\rho-f} \left(\frac{p^2}{a} + \frac{\sigma_e^2}{3b} \right)}, \quad \dot{\varepsilon}_m = \dot{\varepsilon}_0 \left(A \frac{\sigma_e^{(m)}}{\sigma_0} + B \frac{\sigma_e^{(m)^2}}{\sigma_0^2} \right)^p (\varepsilon_m)^{-q}. \tag{20}$$

2.3. Evolution of the phase volume fractions

In the absence of particle dewetting ($\dot{V}_p = 0$), the definition of $\rho = V_p/V$ yields $\dot{\rho} = -(V_p \dot{V}/V^2) = -\rho D_{kk}$. Similarly, $f = V_v/V$ implies that $\dot{f} = (\dot{V}_v/V) - (V_v \dot{V}/V^2) = (1-f)D_{kk}$. Since the presence of porosity can be viewed as some kind of “damage” in the material and any changes in porosity and the volume of the matrix due to elastic deformations are small and fully recoverable, it is assumed that changes in f and ρ are due to the volumetric viscous deformation rate $D_{kk}^v = \dot{\varepsilon}_v$ only (as opposed to the *total* D_{kk}). Therefore, in the absence of particle dewetting, the evolution equations for f and ρ can be written as

$$\dot{\rho} = -\rho \dot{\varepsilon}_v, \quad \dot{f} = \frac{\dot{V}_v}{V} - \frac{V_v \dot{V}}{V^2} = (1-f)\dot{\varepsilon}_v. \tag{21}$$

However, as the material deforms, new voids nucleate by dewetting, thus increasing the void volume fraction (porosity) and decreasing the particle volume fraction as particles are turned into voids. To account for this void nucleation from the existing particles, equations for the void and particle volume fraction rates in Eq. (21) are written as

$$\dot{f} = (1-f)\dot{\varepsilon}_v + \mathbb{Z}(\varepsilon_e)\dot{\varepsilon}_e, \quad \dot{\rho} = -\rho \dot{\varepsilon}_v - \mathbb{Z}(\varepsilon_e)\dot{\varepsilon}_e, \tag{22}$$

where the parameter \mathbb{Z} denotes the amount of particles turned into voids per unit viscous strain ε_e and is so chosen that the nucleation strain follows a normal distribution with mean value ε_N and standard deviation s_N (Chu and Needleman, 1980) that controls the nucleation strain range:

$$\mathbb{Z}(\varepsilon_e) = \frac{\rho_N}{s_N \sqrt{2\pi}} \exp \left[-\frac{1}{2} \left(\frac{\varepsilon_e - \varepsilon_N}{s_N} \right)^2 \right], \tag{23}$$

where ρ_N being the volume fraction of void nucleating particles, i.e., the initial volume fraction of oxidizer particles. Equation (23) dictates that the total volume fraction of particles that can decohere and turn into voids during any straining course equals the amplitude of the Gaussian ρ_0 which is the oxidizer volume fraction. It should be mentioned that Eq. (23) describes a strain-controlled nucleation process in ductile metals at the interface of hard inclusions or particles. The adoption of such an approach in the present work is based on the SEM study of microcracked solid propellants of Cornwell and Schapery (1975) who maintain that cavities in a solid propellant are not unlike those seen around hard particles in a metal–matrix just before failure.

2.4. A viscous model with back stress

As will be demonstrated in Section 4.1, the constitutive model developed in Section 2.2 cannot describe accurately the mechanical behavior of solid propellants in uniaxial tension at different strain rates. In order to

improve the model, we introduce a “deviatoric back stress” α and replace the stress deviator in Eqs. (18)–(20) by the difference $\mathbf{s} - \alpha$.

The constitutive model presented in the following has formal similarities with the “kinematic hardening” models used in the time-independent idealization of plasticity in order to describe the behavior of the material under reversed or cyclic loading. It is emphasized though that in the present model the motivation for the introduction of the back stress α is not the modeling of the Bauschinger effect or the response under cyclic loads; instead, α is introduced in order to describe accurately the “transient” (or “non-stationary”) viscous response of the material (see Section 4.1 below). A similar approach has been used successfully in the past in order to model the non-stationary creep of metal–matrix composites reinforced by continuous elastic fibers, in which α is identified with the stress carried by the fibers (e.g., McLean, 1985; Cheng and Aravas, 1997). The use of back stress models in viscoplasticity is discussed in detail by Rice (1970), who shows that the usual viscoelastic laws that involve hereditary integrals can be stated equivalently in terms of a back stress model.

The modified model now reads as follows:

$$\mathbf{D}^v = \frac{1}{3} \dot{\varepsilon}_v \delta + \dot{\varepsilon}_e \mathbf{N}, \quad \mathbf{N} = \frac{3}{2\Sigma_e} \Sigma, \quad \Sigma = \mathbf{s} - \alpha, \quad \Sigma_e = \sqrt{\frac{3}{2} \Sigma_{ij} \Sigma_{ij}}, \quad (24)$$

where

$$\dot{\varepsilon}_v = \frac{p}{a\mu_m}, \quad \dot{\varepsilon}_e = \frac{\Sigma_e}{3b\mu_m}, \quad a = \frac{2(1-f)(2-2f+3\rho)}{3f(1-f-\rho)}, \quad b = \frac{9f}{4(3+2f)} a, \quad (25)$$

$$\mu_m = \frac{\sigma_e^{(m)}}{3\dot{\varepsilon}_m}, \quad \dot{\varepsilon}_m = \dot{\varepsilon}_0 \left(A \frac{\sigma_e^{(m)}}{\sigma_0} + B \frac{\sigma_e^{(m)^2}}{\sigma_0^2} \right)^p (\varepsilon_m)^{-q}, \quad \sigma_e^{(m)} = \sqrt{\frac{3}{1-\rho-f} \left(\frac{p^2}{a} + \frac{\Sigma_e^2}{3b} \right)}. \quad (26)$$

The evolution equation for α is

$$\overset{\nabla}{\alpha} = H(\varepsilon_e) \mathbf{D}^{v'} - R(\varepsilon_e) \dot{\varepsilon}_e \alpha \quad (27)$$

with

$$H(\varepsilon_e) = H_0 \left(1 + \frac{\varepsilon_e}{\varepsilon_0} \right)^n \quad (28)$$

and

$$R(\varepsilon_e) = R_0 \left(1 + \frac{\varepsilon_e}{\varepsilon_0} \right)^m, \quad (29)$$

where $\mathbf{D}^{v'} = \dot{\varepsilon}_e \mathbf{N}$ is the deviatoric part of \mathbf{D}^v , the two power-law functions H and R control the magnitude of the “hardening” and “dynamic recovery” terms, respectively, ε_0 is a reference strain, and n and m are, respectively, the corresponding powers of hardening and recovery terms.

2.5. The plastic spin

When a back stress is used in a viscoplastic model, one has to distinguish between the continuum spin \mathbf{W} and the substructural spin $\omega = \mathbf{W} - \mathbf{W}^p$, where \mathbf{W}^p is the so-called “plastic spin,” i.e., the spin of the substructure relative to the continuum (Dafalias, 1987, 1988, 1990). In back stress models, the orientation of the substructure is defined by the eigenvectors of α (Lee et al., 1983) and a constitutive equation for the substructural spin ω (or, equivalently, for the plastic spin \mathbf{W}^p) is provided (Aravas, 1994; Dafalias, 1998). A common expression for the plastic spin in such problems is

$$\mathbf{W}^p = h(\varepsilon_e) (\alpha \cdot \mathbf{s} - \mathbf{s} \cdot \alpha). \quad (30)$$

Note that the plastic spin is a measure of the non-co-axiality of \mathbf{s} and α , in the sense that \mathbf{W}^p vanishes if and only if \mathbf{s} and α are co-axial (same principal directions). The physical reasoning behind assigning constitutive equations for the plastic spin for back stress models is discussed in detail by Aravas (1994).

The rate used in the hypoelastic equation (10) and the evolution equation of the back stress (27) is now co-rotational with the substructure, i.e.,

$$\mathbf{D}^e = \mathbf{M}^e : \overset{\circ}{\boldsymbol{\sigma}}, \quad \overset{\circ}{\boldsymbol{\alpha}} = H(\varepsilon_e)\mathbf{D}^{e'} - R(\varepsilon_e)\dot{\varepsilon}_e\boldsymbol{\alpha}, \tag{31}$$

where the notation $\overset{\circ}{\mathbf{A}} = \dot{\mathbf{A}} + \mathbf{A} \cdot \boldsymbol{\omega} - \boldsymbol{\omega} \cdot \mathbf{A}$ is used, and $\boldsymbol{\omega} = \mathbf{W} - \mathbf{W}^p$. The last equations can be written in terms of the Jaumann derivatives as follows:

$$\mathbf{D}^e = \mathbf{M}^e : \overset{\nabla}{\boldsymbol{\sigma}} - \mathbf{M}^e : (\boldsymbol{\sigma} \cdot \mathbf{W}^p - \mathbf{W}^p \cdot \boldsymbol{\sigma}) \tag{32}$$

or

$$\overset{\nabla}{\boldsymbol{\sigma}} = \mathbf{L}^e : \mathbf{D}^e + \boldsymbol{\sigma} \cdot \mathbf{W}^p - \mathbf{W}^p \cdot \boldsymbol{\sigma}, \tag{33}$$

where $\mathbf{L}^e = (\mathbf{M}^e)^{-1}$, and

$$\overset{\nabla}{\boldsymbol{\alpha}} = H(\varepsilon_e)\mathbf{D}^{e'} - R(\varepsilon_e)\dot{\varepsilon}_e\boldsymbol{\alpha} + \boldsymbol{\alpha} \cdot \mathbf{W}^p - \mathbf{W}^p \cdot \boldsymbol{\alpha}. \tag{34}$$

3. Numerical implementation

In a finite element environment, the solution is developed incrementally and the constitutive equations are integrated numerically at the element Gauss integration points. In a displacement-based finite element formulation the solution is deformation driven. Let \mathbf{F} denote the deformation gradient tensor. At a given Gauss point, the solution $(\mathbf{F}_n, \boldsymbol{\sigma}_n, \boldsymbol{\alpha}_n, f_n, \rho_n, \varepsilon_m|_n)$ at time t_n as well as the deformation gradient \mathbf{F}_{n+1} at time $t_{n+1} = t_n + \Delta t$ are known and the problem is to determine $(\boldsymbol{\sigma}_{n+1}, \boldsymbol{\alpha}_{n+1}, f_{n+1}, \rho_{n+1}, \varepsilon_m|_{n+1})$.

The time variation of the deformation gradient \mathbf{F} during the time increment $[t_n, t_{n+1}]$ can be written as

$$\mathbf{F}(t) = \Delta\mathbf{F}(t) \cdot \mathbf{F}_n = \mathbf{R}(t) \cdot \mathbf{U}(t) \cdot \mathbf{F}_n, \quad t_n \leq t \leq t_{n+1}, \tag{35}$$

where $\mathbf{R}(t)$ and $\mathbf{U}(t)$ are the rotation and right stretch tensors associated with $\Delta\mathbf{F}(t)$. The corresponding deformation rate $\mathbf{D}(t)$ and spin $\mathbf{W}(t)$ tensors can be written as

$$\mathbf{D}(t) \equiv [\dot{\mathbf{F}}(t) \cdot \mathbf{F}^{-1}(t)]_s = [\Delta\dot{\mathbf{F}}(t) \cdot \Delta\mathbf{F}^{-1}(t)]_s, \tag{36}$$

$$\mathbf{W}(t) \equiv [\dot{\mathbf{F}}(t) \cdot \mathbf{F}^{-1}(t)]_a = [\Delta\dot{\mathbf{F}}(t) \cdot \Delta\mathbf{F}^{-1}(t)]_a, \tag{37}$$

where the subscripts s and a denote the symmetric and anti-symmetric parts, respectively, of a tensor.

If it is assumed that the Lagrangian triad associated with $\Delta\mathbf{F}(t)$ (i.e., the eigenvectors of $\mathbf{U}(t)$) remains fixed in the time interval $[t_n, t_{n+1}]$, it can be shown readily that

$$\mathbf{D}(t) = \mathbf{R}(t) \cdot \dot{\mathbf{E}}(t) \cdot \mathbf{R}^T(t), \quad \mathbf{W}(t) = \dot{\mathbf{R}}(t) \cdot \mathbf{R}^T(t) \tag{38}$$

and

$$\overset{\nabla}{\boldsymbol{\sigma}}(t) = \mathbf{R}(t) \cdot \dot{\hat{\boldsymbol{\sigma}}}(t) \cdot \mathbf{R}^T(t), \quad \overset{\nabla}{\boldsymbol{\alpha}}(t) = \mathbf{R}(t) \cdot \dot{\hat{\boldsymbol{\alpha}}}(t) \cdot \mathbf{R}^T(t), \tag{39}$$

where $\mathbf{E}(t) = \ln \mathbf{U}(t)$ is the logarithmic strain associated with the increment, and

$$\hat{\boldsymbol{\sigma}}(t) = \mathbf{R}^T(t) \cdot \boldsymbol{\sigma}(t) \cdot \mathbf{R}(t), \quad \hat{\boldsymbol{\alpha}}(t) = \mathbf{R}^T(t) \cdot \boldsymbol{\alpha}(t) \cdot \mathbf{R}(t). \tag{40}$$

It is noted that at the start of the increment ($t = t_n$):

$$\Delta\mathbf{F}_n = \mathbf{R}_n = \mathbf{U}_n = \boldsymbol{\delta}, \quad \hat{\boldsymbol{\sigma}}_n = \boldsymbol{\sigma}_n, \quad \hat{\boldsymbol{\alpha}}_n = \boldsymbol{\alpha}_n, \quad \mathbf{E}_n = \mathbf{0}, \tag{41}$$

whereas at the end of the increment ($t = t_{n+1}$):

$$\Delta\mathbf{F}_{n+1} = \mathbf{F}_{n+1} \cdot \mathbf{F}_n^{-1} = \mathbf{R}_{n+1} \cdot \mathbf{U}_{n+1} = \text{known}, \quad \mathbf{E}_{n+1} = \ln \mathbf{U}_{n+1} = \text{known}. \tag{42}$$

Then, over the time interval $[t_n, t_{n+1}]$, the constitutive equations can be written in the form:

$$\dot{\mathbf{E}} = \dot{\mathbf{E}}^e + \dot{\mathbf{E}}^p, \tag{43}$$

$$\dot{\hat{\boldsymbol{\sigma}}} = \mathbf{L}^e : \dot{\mathbf{E}}^e + h(2\hat{\boldsymbol{\sigma}} \cdot \hat{\boldsymbol{\alpha}} \cdot \hat{\boldsymbol{\sigma}} - \hat{\boldsymbol{\sigma}}^2 \cdot \hat{\boldsymbol{\alpha}} - \hat{\boldsymbol{\alpha}} \cdot \hat{\boldsymbol{\sigma}}^2), \tag{44}$$

$$\dot{\mathbf{E}}^v = \frac{1}{3}\dot{\varepsilon}_v \boldsymbol{\delta} + \dot{\varepsilon}_e \hat{\mathbf{N}}, \quad \hat{\mathbf{N}} = \frac{3}{2\Sigma_e} \hat{\boldsymbol{\Sigma}}, \quad \hat{\boldsymbol{\Sigma}} = \hat{\mathbf{s}} - \hat{\boldsymbol{\alpha}}, \quad \Sigma_e = \sqrt{\frac{3}{2} \hat{\Sigma}_{ij} \hat{\Sigma}_{ij}}, \tag{45}$$

$$\dot{\hat{\boldsymbol{\alpha}}} = H(\varepsilon_e) \dot{\mathbf{E}}^{v'} - R(\varepsilon_e) \dot{\varepsilon}_e \hat{\boldsymbol{\alpha}} + h(\hat{\boldsymbol{\alpha}}^2 \cdot \hat{\mathbf{s}} + \hat{\mathbf{s}} \cdot \hat{\boldsymbol{\alpha}}^2 - 2\hat{\boldsymbol{\alpha}} \cdot \hat{\mathbf{s}} \cdot \hat{\boldsymbol{\alpha}}), \tag{46}$$

where

$$\dot{\varepsilon}_v = \frac{p}{a\mu_m}, \quad \dot{\varepsilon}_e = \frac{\Sigma_e}{3b\mu_m}, \quad a = \frac{2(1-f)(2-2f+3\rho)}{3f(1-f-\rho)}, \quad b = \frac{9f}{4(3+2f)}a, \tag{47}$$

$$\mu_m = \frac{\sigma_e^{(m)}}{3\dot{\varepsilon}_m}, \quad \dot{\varepsilon}_m = \dot{\varepsilon}_0 \left(A \frac{\sigma_e^{(m)}}{\sigma_0} + B \frac{\sigma_e^{(m)^2}}{\sigma_0^2} \right)^p (\varepsilon_m)^{-q}, \quad \sigma_e^{(m)} = \sqrt{\frac{3}{1-\rho-f} \left(\frac{p^2}{a} + \frac{\Sigma_e^2}{3b} \right)}. \tag{48}$$

The evolution of the volume fractions of the phases is given by

$$\dot{f} = (1-f)\dot{\varepsilon}_v + \mathbb{Z}(\varepsilon_e)\dot{\varepsilon}_e, \quad \dot{\rho} = -\rho\dot{\varepsilon}_v - \mathbb{Z}(\varepsilon_e)\dot{\varepsilon}_e. \tag{49}$$

The co-rotational rates $\overset{\nabla}{\boldsymbol{\sigma}}$ and $\overset{\nabla}{\boldsymbol{\alpha}}$ in the original equations are now replaced by the usual material time derivatives $\dot{\hat{\boldsymbol{\sigma}}}$ and $\dot{\hat{\boldsymbol{\alpha}}}$. This is a consequence of the assumption that the Lagrangian triad associated with $\Delta\mathbf{F}$ remains fixed in the time interval $[t_n, t_{n+1}]$ so that $\mathbf{W} = \dot{\mathbf{R}} \cdot \mathbf{R}^T$, which implies in turn that $\overset{\nabla}{\boldsymbol{\sigma}} = \mathbf{R} \cdot \dot{\hat{\boldsymbol{\sigma}}} \cdot \mathbf{R}^T$. It should be noted that the aforementioned assumption on the Lagrangian triad is less “severe” than the usual assumption of “constant strain rate” over the time increment.

Equation (43) can be integrated exactly:

$$\Delta\mathbf{E} = \Delta\mathbf{E}^e + \Delta\mathbf{E}^v, \tag{50}$$

where the notation $\Delta A = A_{n+1} - A_n$ is used.

In order to simplify the calculations, we use a forward Euler scheme for the numerical integration of the evolution equations of the volume fractions Eq. (49):

$$f_{n+1} = f_n + (1-f_n)\Delta\varepsilon_v|_n + \mathbb{Z}(\varepsilon_e|_n)\Delta\varepsilon_e|_n \equiv f = \text{known}, \tag{51}$$

$$\rho_{n+1} = \rho_n - \rho_n\Delta\varepsilon_v|_n - \mathbb{Z}(\varepsilon_e|_n)\Delta\varepsilon_e|_n \equiv \rho = \text{known}, \tag{52}$$

$$c_m|_{n+1} = 1 - \rho_{n+1} - f_{n+1} = \text{known} \tag{53}$$

with

$$\Delta\varepsilon_v|_n = \Delta t \left(\frac{p}{a\mu_m} \right)_n, \quad \Delta\varepsilon_e|_n = \Delta t \left(\frac{\Sigma_e}{3b\mu_m} \right)_n. \tag{54}$$

We also determine

$$a_{n+1} = \frac{2(1-f_{n+1})(2-2f_{n+1}+3\rho_{n+1})}{3f_{n+1}(1-f_{n+1}-\rho_{n+1})} = \text{known}, \quad b_{n+1} = \frac{9f_{n+1}}{4(3+2f_{n+1})}a_{n+1} = \text{known}. \tag{55}$$

For the numerical integration of the elasticity Eq. (44), and the evolution equation for the back stress equation (46), a forward Euler scheme is used in the form

$$\hat{\boldsymbol{\sigma}}_{n+1} = \boldsymbol{\sigma}^e - \mathbf{L}_n^e : \Delta\mathbf{E}^v + h_n(2\hat{\boldsymbol{\sigma}}_n \cdot \hat{\boldsymbol{\alpha}}_n \cdot \hat{\boldsymbol{\sigma}}_n - \hat{\boldsymbol{\sigma}}_n^2 \cdot \hat{\boldsymbol{\alpha}}_n - \hat{\boldsymbol{\alpha}}_n \cdot \hat{\boldsymbol{\sigma}}_n^2)\Delta t, \tag{56}$$

where $\boldsymbol{\sigma}^e = \boldsymbol{\sigma}_n + \mathbf{L}_n^e : \Delta\mathbf{E}$ is known is the “elastic predictor,” and

$$\hat{\boldsymbol{\alpha}}_{n+1} = \hat{\boldsymbol{\alpha}}_n + H_n\Delta\mathbf{E}^{v'} - R_n\Delta\varepsilon_e\hat{\boldsymbol{\alpha}}_n - h_n(2\hat{\boldsymbol{\alpha}}_n \cdot \hat{\mathbf{s}}_n \cdot \hat{\boldsymbol{\alpha}}_n - \hat{\boldsymbol{\alpha}}_n^2 \cdot \hat{\mathbf{s}}_n - \hat{\mathbf{s}}_n \cdot \hat{\boldsymbol{\alpha}}_n^2). \tag{57}$$

A backward Euler scheme is used for the integration of the flow rule, and the evolution equation of ε_m :

$$\Delta \mathbf{E}^v = \frac{1}{3} \Delta \varepsilon_v \boldsymbol{\delta} + \Delta \varepsilon_e \hat{\mathbf{N}}_{n+1}, \quad \frac{\Delta \varepsilon_m}{\Delta t} = \dot{\varepsilon}_0 \left(A \frac{\sigma_e^{(m)}}{\sigma_0} \Big|_{n+1} + B \frac{\sigma_e^{(m)2}}{\sigma_0} \Big|_{n+1} \right)^r (\varepsilon_m|_n + \Delta \varepsilon_m)^{-q} \quad (58)$$

with

$$\hat{\mathbf{N}}_{n+1} = \frac{3}{2 \Sigma_e|_{n+1}} \hat{\Sigma}_{n+1}, \quad \hat{\Sigma}_{n+1} = \hat{s}_{n+1} - \hat{\alpha}_{n+1}, \quad \Sigma_e|_{n+1} = \sqrt{\frac{3}{2} \hat{\Sigma}_{ij}|_{n+1} \hat{\Sigma}_{ij}|_{n+1}}, \quad (59)$$

$$\Delta \varepsilon_v = \frac{p_{n+1}}{a \mu_m|_{n+1}} \Delta t, \quad \Delta \varepsilon_e = \frac{\Sigma_e|_{n+1}}{3b \mu_m|_{n+1}} \Delta t, \quad \mu_m|_{n+1} = \frac{\sigma_e^{(m)}|_{n+1}}{3 \dot{\varepsilon}_m|_{n+1}}, \quad (60)$$

$$\sigma_e^{(m)}|_{n+1} = \sqrt{\frac{3}{c_m|_{n+1}} \left(\frac{p_{n+1}^2}{a_{n+1}} + \frac{\Sigma_e|_{n+1}^2}{3b_{n+1}} \right)}. \quad (61)$$

It should be noted that both the forward and backward Euler schemes are “first-order” methods. However, use of the forward Euler method for the integration of the “flow rule” limits the size of the time increment that can be used, especially in problems where the principal directions of stress rotate substantially over an increment. Integration of the flow rule via the backward Euler method allows for the use of more reasonable time increments (Kailasam et al., 2000; Aravas and Ponte Castañeda, 2004).

We treat $\Delta \mathbf{E}^v$ as the primary unknown, and use the flow rule as the basic equation for its determination:

$$\mathbf{F}(\Delta \mathbf{E}^v) = \Delta \mathbf{E}^v - \left[\frac{p_{n+1}}{3a_{n+1} \mu_m|_{n+1}} \boldsymbol{\delta} + \frac{1}{2b_{n+1} \mu_m|_{n+1}} (\hat{\mathbf{s}}_{n+1} - \hat{\boldsymbol{\alpha}}_{n+1}) \right] \Delta t = \mathbf{0}. \quad (62)$$

In the last equation, all quantities on the right-hand side are determined in terms of $\Delta \mathbf{E}^v$:

$$\hat{\boldsymbol{\sigma}}_{n+1}(\Delta \mathbf{E}^v) = \boldsymbol{\sigma}^e - \mathbf{L}_n^e : \Delta \mathbf{E}^v + h_n [\hat{\boldsymbol{\sigma}}_n \cdot (\hat{\boldsymbol{\alpha}}_n \cdot \hat{\mathbf{s}}_n - \hat{\mathbf{s}}_n \cdot \hat{\boldsymbol{\alpha}}_n) - (\hat{\boldsymbol{\alpha}}_n \cdot \hat{\mathbf{s}}_n - \hat{\mathbf{s}}_n \cdot \hat{\boldsymbol{\alpha}}_n) \cdot \hat{\boldsymbol{\sigma}}_n] \Delta t, \quad (63)$$

$$p_{n+1}(\Delta \mathbf{E}^v) = \frac{1}{3} \hat{\boldsymbol{\sigma}}_{n+1} : \boldsymbol{\delta}, \quad \hat{\mathbf{s}}_{n+1}(\Delta \mathbf{E}^v) = \hat{\boldsymbol{\sigma}}_{n+1} - p_{n+1} \boldsymbol{\delta}, \quad (64)$$

$$\Delta \mathbf{E}^{v'}(\Delta \mathbf{E}^v) = \Delta \mathbf{E}^v - \frac{1}{3} (\Delta \mathbf{E}^v : \boldsymbol{\delta}) \boldsymbol{\delta}, \quad \Delta \varepsilon_e(\Delta \mathbf{E}^v) = \sqrt{\frac{2}{3} \Delta \mathbf{E}^{v'} : \Delta \mathbf{E}^{v'}}, \quad (65)$$

$$\hat{\boldsymbol{\alpha}}_{n+1}(\Delta \mathbf{E}^v) = \hat{\boldsymbol{\alpha}}_n + H_n \Delta \mathbf{E}^{v'} - R_n \Delta \varepsilon_e \hat{\boldsymbol{\alpha}}_n - h_n (2 \hat{\boldsymbol{\alpha}}_n \cdot \hat{\mathbf{s}}_n \cdot \hat{\boldsymbol{\alpha}}_n - \hat{\boldsymbol{\alpha}}_n^2 \cdot \hat{\mathbf{s}}_n - \hat{\mathbf{s}}_n \cdot \hat{\boldsymbol{\alpha}}_n^2), \quad (66)$$

$$\Sigma_e|_{n+1}(\Delta \mathbf{E}^v) = \sqrt{\frac{3}{2} (\hat{s}_{ij} - \hat{\alpha}_{ij})_{n+1} (\hat{s}_{ij} - \hat{\alpha}_{ij})_{n+1}}, \quad \sigma_e^{(m)}|_{n+1}(\Delta \mathbf{E}^v) = \sqrt{\frac{3}{c_m|_{n+1}} \left(\frac{p_{n+1}^2}{a_{n+1}} + \frac{\Sigma_e|_{n+1}^2}{3b_{n+1}} \right)}, \quad (67)$$

$$\frac{\Delta \varepsilon_m(\Delta \mathbf{E}^v)}{\Delta t} = \dot{\varepsilon}_0 \left(A \frac{\sigma_e^{(m)}}{\sigma_0} \Big|_{n+1} + B \frac{\sigma_e^{(m)2}}{\sigma_0} \Big|_{n+1} \right)^r (\varepsilon_m|_n + \Delta \varepsilon_m(\Delta \mathbf{E}^v))^{-q}, \quad (68)$$

$$\varepsilon_m|_{n+1}(\Delta \mathbf{E}^v) = \varepsilon_m|_n + \Delta \varepsilon_m(\Delta \mathbf{E}^v), \quad \dot{\varepsilon}_m|_{n+1}(\Delta \mathbf{E}^v) = \frac{\Delta \varepsilon_m}{\Delta t}, \quad \mu_m|_{n+1}(\Delta \mathbf{E}^v) = \frac{\sigma_e^{(m)}|_{n+1}}{3 \dot{\varepsilon}_m|_{n+1}}. \quad (69)$$

Equation (62) is solved for $\Delta \mathbf{E}^v$ by using Newton’s method. In the process of iteration for a given $\Delta \mathbf{E}^v$, a local Newton loop is used to solve Eq. (68) for $\Delta \varepsilon_m$.

Once $\Delta \mathbf{E}^v$ is found, $\boldsymbol{\sigma}_{n+1}$ and $\boldsymbol{\alpha}_{n+1}$ are computed from

$$\boldsymbol{\sigma}_{n+1} = \mathbf{R}_{n+1} \cdot \hat{\boldsymbol{\sigma}}_{n+1} \cdot \mathbf{R}_{n+1}^T, \quad \boldsymbol{\alpha}_{n+1} = \mathbf{R}_{n+1} \cdot \hat{\boldsymbol{\alpha}}_{n+1} \cdot \mathbf{R}_{n+1}^T, \quad (70)$$

which completes the integration process.

4. Applications

The constitutive model developed in the previous sections is implemented in the ABAQUS general purpose finite element program (Hibbitt, 1977). This code provides a general interface so that a particular constitutive model can be introduced as a “user interface.” The integration of the constitutive equations is carried out using the algorithm presented in Section 3. The finite element formulation is based on the weak form of the momentum balance, the solution is carried out incrementally, and the discretized nonlinear equations are solved using Newton’s method. The Jacobian of the equilibrium Newton-loop requires the so-called “linearization moduli” of the algorithm, which are reported in Xu (2008).

Since there are no available experimental data yet for stress states in which the stress tensor is not co-axial with the back stress, we assume in the following that $h = 0$ in Eq. (30), i.e., $\mathbf{W}^p = 0$. It is emphasized though that, when such data become available, the effects of the plastic spin can be accounted for as described in Section 2.5.

4.1. Uniaxial tension and shear relaxation

As specific data from a real-world solid propellant were not available, we assumed that the initial value of the volume fraction of particles (oxidizer and fuel) was $\rho_0 = 0.715$ and the initial volume fraction of the oxidizer particles, i.e., those particles in the model that could turn into voids upon straining, was $\rho_N = 0.615$. These numbers correspond to an initial volume fraction for the fuel equal to 0.100. We also assumed that the propellant had a small amount of an initial porosity $f_0 = 0.01$ which in a real-world material can be attributed to long-term chemical reactions. It is well known that propellants stored for a long time experience degradation from chemical changes in their microstructure (Sutton, 1986).

The viscous model for the uniaxial strain rate-stress equation (17) for the matrix, the two parameters ε_N , and s_N in the statistical model of Eq. (23) for particle dewetting, and the “hardening” and “recovery” functions in the back stress evolution Eq. (27) were calibrated by matching the model predictions with experimental data of Özüpek and Becker (1992) from solid propellant uniaxial tension tests under constant strain rate and shear relaxation tests. This calibration yielded $\mu_m = 0.39$ MPa for the elastic shear modulus of the matrix; $\dot{\varepsilon}_0 = 1.0 \text{ s}^{-1}$, $\sigma_0 = 1.0$ MPa, $A = 0.1$, $B = 7.5$, $p = 3.75$, $q = 2.5$ for the matrix viscous response; $\varepsilon_N = 0.3$, and $s_N = 0.2$ for the characteristics of particle dewetting; and two sets of constants for the “hardening” and “recovery” rate parameters in the evolution of the back stress: (i) $H_0 = 0.22$ MPa, $\varepsilon_0 = 1.0$, $n = 0.3$, $R_0 = 5$, and $m = 0$, (ii) $H_0 = 0.22$ MPa, $\varepsilon_0 = 1.0$, $n = 0$, $R_0 = 0$, and $m = 0$. Set (i) represents nonlinear “hardening” rate with constant “recovery” rate and set (ii) constant “hardening” rate with no “recovery.” These choices for the hardening and recovery forms which are discussed below gave the best fit to the experimental data.

Fig. 2 compares the model predictions with the data of Özüpek and Becker (1992) in uniaxial tension at several strain rates. The stress Σ in response to four constant applied engineering strain rates is plotted as a function of the logarithmic strain E . Given the wide range of loading rates, one may deem the predictions quite acceptable for both sets of hardening and recovery parameters.

It should be emphasized that, if no back stress is used ($H_0 = 0$, $R_0 = 0$), then the predictions of the model do not agree with the experimental data. One of the reasons for this difficulty is the use of the additive split of Eq. (3), which is based on the assumption that the elastic and viscous deformation rates can be treated independently. Use of the back stress improves substantially the predictions of the model and accounts, in a sense, for the evolution of the microstructure as the material deforms. As mentioned in Section 2.4 above, the use of the back stress in this case is not related to the Bauschinger effect of any cyclic loading; instead, it is used to model the “transient” (non-“steady-state”) creep of the composite.

Fig. 3 shows the comparison of the model performance in shear with shear relaxation data. The shear stress Σ_{12} was calculated in response to an imposed constant shear strain E_{12} on the element. The model underestimates the shear relaxation modulus $G(t) = \Sigma_{12}(t)/E_{12}$ at small times t and overestimates it for large t . The source of this difference is identified again with the additive Maxwell-type decomposition $\mathbf{D} = \mathbf{D}^e + \mathbf{D}^p$ and the creep Eq. (17) used to describe the nonlinear viscous response of the matrix material. The experimental data (Özüpek and Becker, 1992) show that $G(t)$ approaches a constant value at large times, whereas all Maxwell-type models are such that $G(t)$ vanishes asymptotically as $t \rightarrow \infty$.

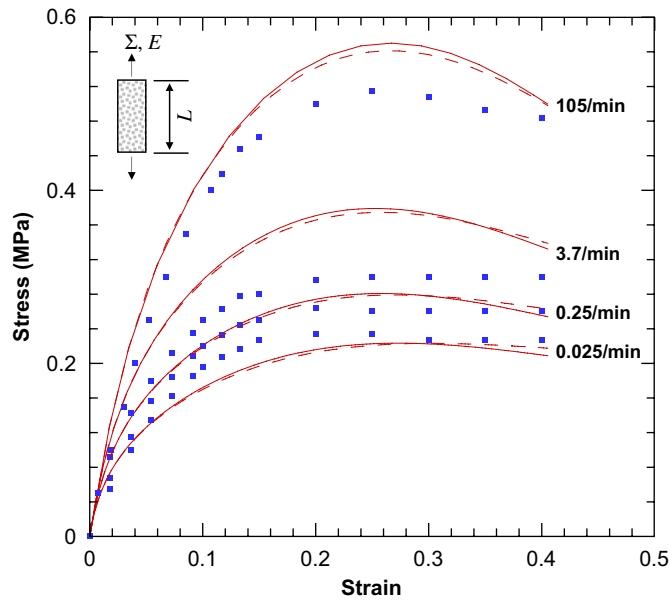


Fig. 2. Comparison of model predictions in uniaxial tension tests at constant strain rates of 105, 3.7, 0.25, and 0.025 min⁻¹ with back stress characterized by (a) $H_0 = 0.22$ MPa, $n = 0.3$, $R_0 = 5.0$, and $m = 0.0$ (solid lines); (b) $H_0 = 0.22$ MPa, $n = 0.0$, $R_0 = 0.0$, and $m = 0.0$ (dash lines). Superposed data points are corresponding experimental data.

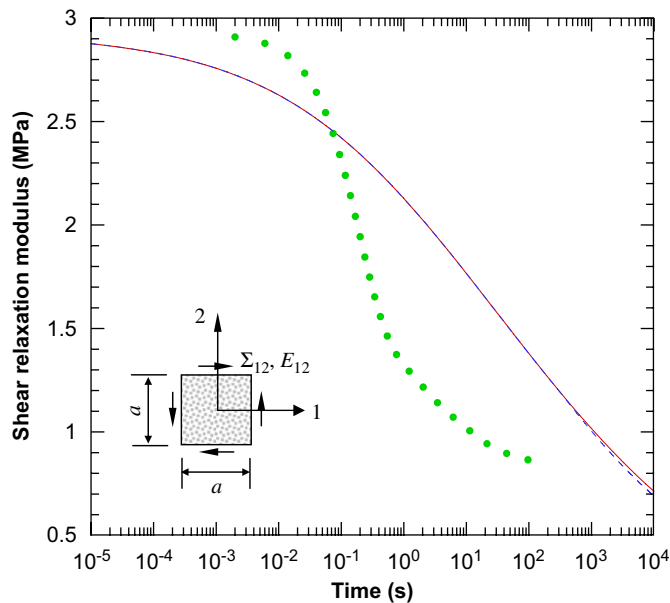


Fig. 3. Comparison of model predictions in shear relaxation with back stress characterized by (a) $H_0 = 0.22$ MPa, $n = 0.3$, $R_0 = 5.0$, and $m = 0.0$ (dash line); (b) $H_0 = 0.22$ MPa, $n = 0.0$, $R_0 = 0.0$, and $m = 0.0$ (solid line). Superposed data points are corresponding experimental data.

The interplay between the relative magnitudes of the hardening and recovery terms in the evolution of the back stress and its effect on the uniaxial tension response is explored in Figs. 4 and 5 under constant strain rate of 105 min⁻¹. For a given constant recovery rate described by $m = 0$ and $R_0 = 5.0$, Fig. 4 clearly shows that the hardening exponent n in Eq. (28) controls the hardening response at large strains, as expected. As n increases from 0 to 1, the hardening rate varies from constant, H_0 , to linear, $H_0(1 + \epsilon_e/\epsilon_0)$. It seems that the

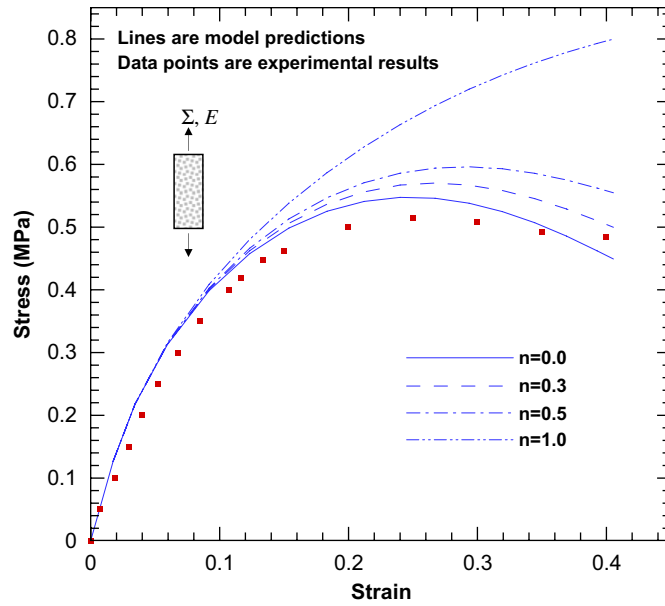


Fig. 4. Parametric study of the effect of hardening exponent n on the stress response in uniaxial tension test at constant strain rate of 105 min^{-1} : $H_0 = 0.22 \text{ MPa}$, $R_0 = 5.0$, and $m = 0$.

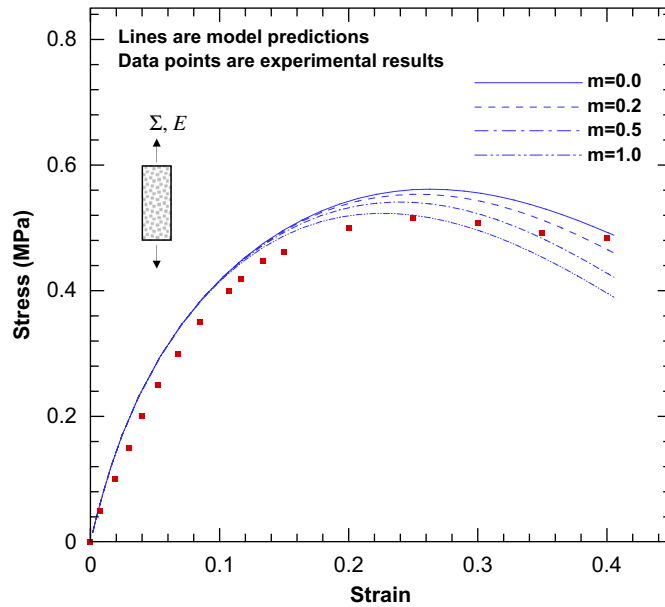


Fig. 5. Parametric study of the effect of recovery exponent m on the stress response in uniaxial tension test at constant strain rate of 105 min^{-1} : $H_0 = 0.22 \text{ MPa}$, $n = 0.3$, and $R_0 = 5.0$.

combination of constant hardening and recovery rates does well in reproducing the experimental data except at very large strains (>0.35) at which it seems that it cannot continue to successfully counter the softening due to dewetting. Thus the combination of the nonlinear hardening rate, $H_0 = 0.22 \text{ MPa}$, $n = 0.3$, with constant recovery is deemed as a better choice for the overall response. Fig. 5 shows the effect of recovery rate on the uniaxial response under the given nonlinear hardening rate: $H_0 = 0.22 \text{ MPa}$, $n = 0.3$. Clearly, at large strains, large recovery exponents are associated with predictions that are markedly softer than the experimental ones,

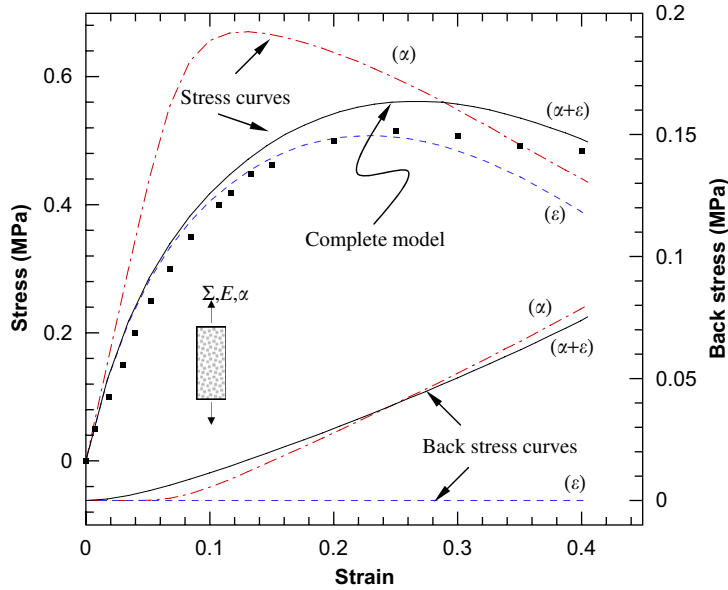


Fig. 6. Predictions in uniaxial tension as influenced by the strain-dependent part of the matrix viscous response (cf. Eq. (17)) and the back stress: curves (α) denote predictions in the presence of back stress but with no strain-dependent term; curves (ε) predictions with strain-dependent term and no back stress; curves $(\alpha + \varepsilon)$ with strain-dependent term and back stress, that is, complete model. The simulations were carried out with $H_0 = 0.22$ MPa, $n = 0.0$, $R_0 = 0.0$, and $m = 0.0$. Superposed are experimental data under constant strain rate of 105 min^{-1} .

and this is the reason that the choice of set (i) with constant recovery ($m = 0$, $R_0 = 5.0$) was made for the calibration of the model. Interestingly, as shown in Fig. 6, another calibration, that is, of constant hardening rate with no recovery at all ($n = 0$, $H_0 = 0.22$ MPa, $R_0 = 0$) also does well in reproducing the experimental response. For this reason and because of its simplicity, we adopted set (ii) of a constant hardening rate with no recovery ($n = 0$, $H_0 = 0.22$ MPa, $R_0 = 0$) for the description of the evolution law for the back stress in all subsequent calculations.

As has been discussed in Sections 2.2 and 2.4, two important ingredients of the present constitutive law are: (i) the suggested model of Eq. (17) for the viscous response of the matrix and (ii) the presence of a back stress, Eq. (27), to describe the change of the propellant microstructure with straining. In Eq. (17) the viscous strain rate of the matrix $\dot{\varepsilon}_m$ depends on stress and is proportional to $(\varepsilon_m)^{-q}$ with $q > 0$. This type of dependence of $\dot{\varepsilon}_m$ on ε_m is known in the literature as “strain softening creep”, since, for a given stress level, $\dot{\varepsilon}_m$ decreases as ε_m increases. The results presented in Fig. 6 for the case of uniaxial tension response of the propellant at strain rate (105 min^{-1}) make it clear that, if no back stress is used, the predicted response at strains larger than 0.25 is softer than the experimentally observed, (curve (ε) in Fig. 6). For this reason the back stress was incorporated to impart the necessary counteracting hardening in the response at large strains. Introduction of the back stress brings the response of the propellant in line with the experiment for strains up to 0.4 (curve $(\alpha + \varepsilon)$ in Fig. 6). On the other hand, one cannot reproduce the experimental response through a constitutive law in which the strain-dependent term $(\varepsilon_m)^q$ in the response of the matrix is neglected altogether. Clearly, the presence of a back stress alone in the constitutive law produces too stiff a response in particular at the early stages of the deformation (curve (α) in Fig. 6).

The associated evolution of porosity f , particle volume fraction ρ , and dilatation ε_v upon straining predicted by the model in uniaxial tension is shown in Fig. 7. In Fig. 7a, f and ρ are plotted against the macroscopic strain E at strain rates $\dot{E} = 105, 3.7, 0.25$, and 0.025 min^{-1} . Before straining, the sum of the volume fractions of particles and voids is $\rho_0 + f_0 = 0.725$. At strain 0.4 and strain rate 0.025 min^{-1} , the corresponding sum $\rho + f$ is equal to 0.74. This difference of about 3% indicates that the porosity increase is mainly due to particle dewetting (void nucleation) and is only slightly due to the enlargement of the voids by viscous deformation. Fig. 7b shows the macroscopic dilatation ε_v as a function of E and \dot{E} . At small strains ($E < 0.1$), the dilatation

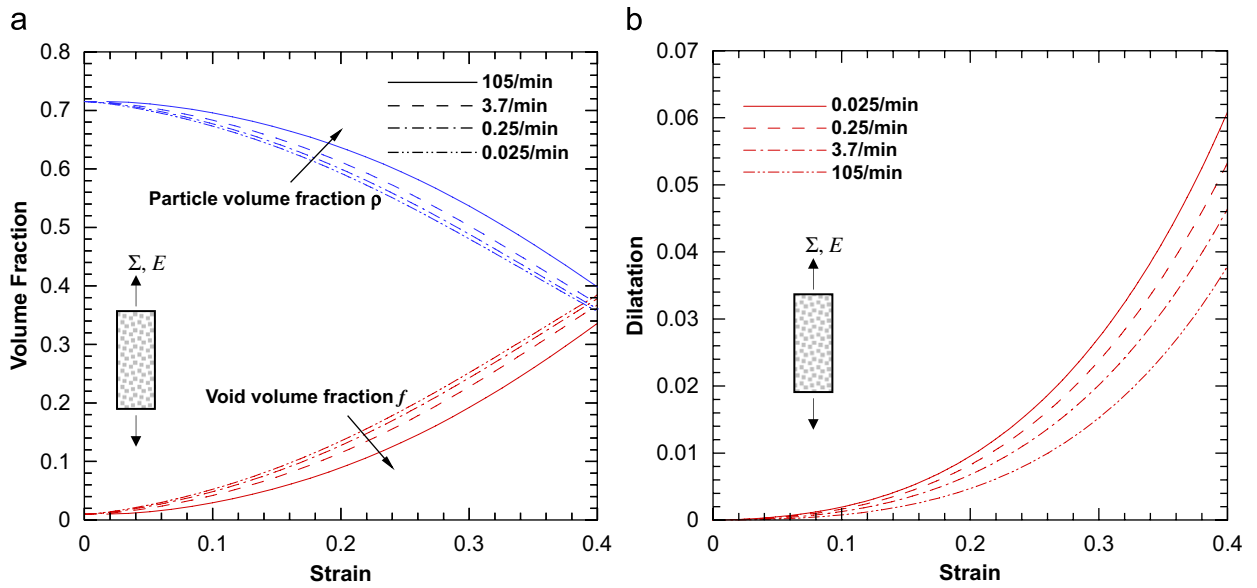


Fig. 7. (a) Plot of the void volume fraction f and particle volume fraction ρ as a function of applied macroscopic strain in uniaxial tension at various applied strain rates; (b) plot of the macroscopic dilatation. For both (a) and (b) the model parameters were: $H_0 = 0.22$ MPa, $n = 0.0$, $R_0 = 0.0$, and $m = 0.0$.

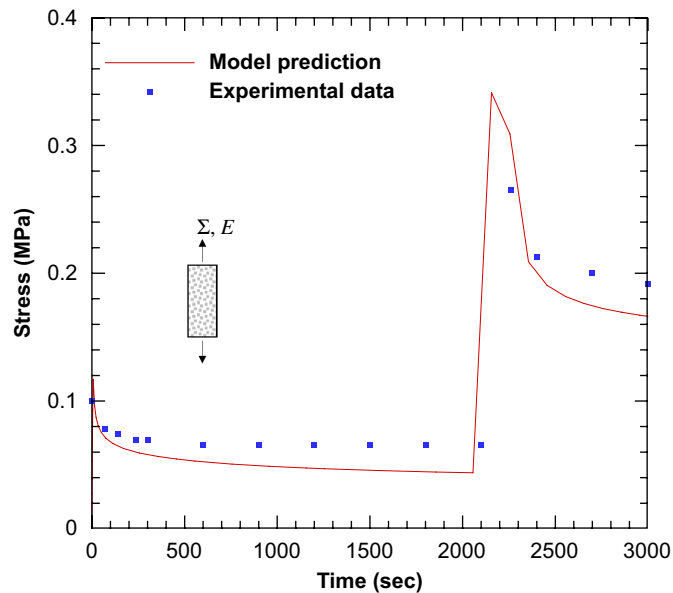


Fig. 8. Comparison of model prediction with experimental data in uniaxial tension under a complex loading path: the specimen was first strained to macroscopic strain of 0.03 at constant strain rate 0.25 min^{-1} , then relaxed under strain 0.03 for 35 min, then re-loaded to strain 0.5 at a constant strain rate of 0.25 min^{-1} , and lastly relaxed under strain 0.5 for 13 min. The material data were: $H_0 = 0.22$ MPa, $n = 0.0$, $R_0 = 0.0$, and $m = 0.0$.

is small because the void volume fraction is quite small and the propellant is nearly incompressible. At larger strains, void growth induces macroscopic compressibility and this is also manifested in the strain rate dependence of the macroscopic dilatation.

Having explored the characteristics of the present model in uniaxial tension and shear relaxation, we investigated the model performance in more complex uniaxial straining situations. Fig. 8 shows the model

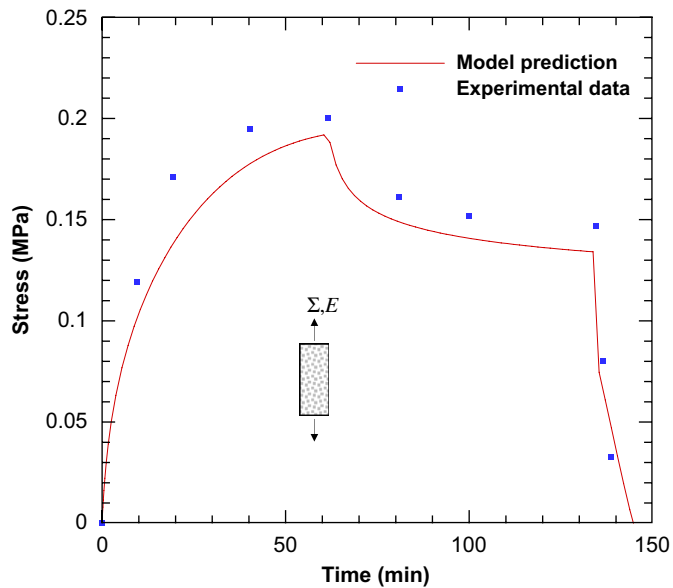


Fig. 9. Comparison of model prediction with experimental data in uniaxial tension under a complex loading path: The specimen was first strained to macroscopic strain of 0.3 at constant strain rate 0.005 min^{-1} , then relaxed under strain 0.3 for 73 min, and lastly unloaded at a constant strain rate of 0.05 min^{-1} . The material data were: $H_0 = 0.22 \text{ MPa}$, $n = 0.0$, $R_0 = 0.0$, and $m = 0.0$.

predictions compared with the experimental data of Özüpek and Becker (1992) over a path that involves: (i) application of a strain 0.03 at a constant strain rate 0.25 min^{-1} , (ii) stress relaxation under strain 0.03 for 2100 s, (iii) re-straining to a strain 0.5 at a constant strain rate 0.25 min^{-1} , (iv) stress relaxation under strain 0.5. Similarly Fig. 9 shows the comparison of the model predictions with the experiment under a path of: (i) application of a strain 0.3 at a rate 0.005 min^{-1} , (ii) stress relaxation under strain 0.3 for 73 min, and (iii) complete unloading at a constant strain rate of 0.05 min^{-1} . Both Figs. 8 and 9 show that the model predictions compare with the experimental data of Özüpek and Becker (1992) satisfactorily. Again, during the relaxation stage, the presence of the strain-dependent term in the matrix response assists the relaxation process while the presence of the back stress holds the specimen from over-relaxing. The synergistic effect brings about the optimum relaxation response as shown by the two figures.

4.2. Mechanical response of a compact tension fracture specimen

Measurement of the fracture toughness of solid propellant materials is a complex and yet unresolved problem. This is partly due to the lack of an adequate constitutive theory for the calculation of the stress and strain fields ahead of a crack tip. Owing to the lack of such a theory, no parameters potentially descriptive of the crack tip fields have been identified. In fact, the open literature does not show a systematic attempt by the scientific community to come up with experimentally validated criteria for fracture of solid propellants under large straining. In other words, no intensive fracture mechanics effort similar to that made in the 70 and 80 s for the establishment of the J -integral as a criterion for ductile fracture of metals and alloys has been mounted for solid propellant materials. Also, specific testing details such as the identification of the location of a natural crack tip in a damaged solid propellant should not be overlooked as sources for the slow development of fracture theories for solid propellant materials. Unlike the case of metallic systems in which a natural crack is easily inserted through fatigue pre-cracking, propellant test-pieces may fail completely under such a similar process.

In this section, we use the constitutive theory we developed in this work to study the response of a compact tension fracture mechanics specimen. We demonstrate that the macroscopic response of the specimen may depend on the loading path. The underlying issue here is the effect of pre-loading, possibly arising from crack introduction, on the fracture response of solid propellant materials (Little and Rice, 2004). Through our

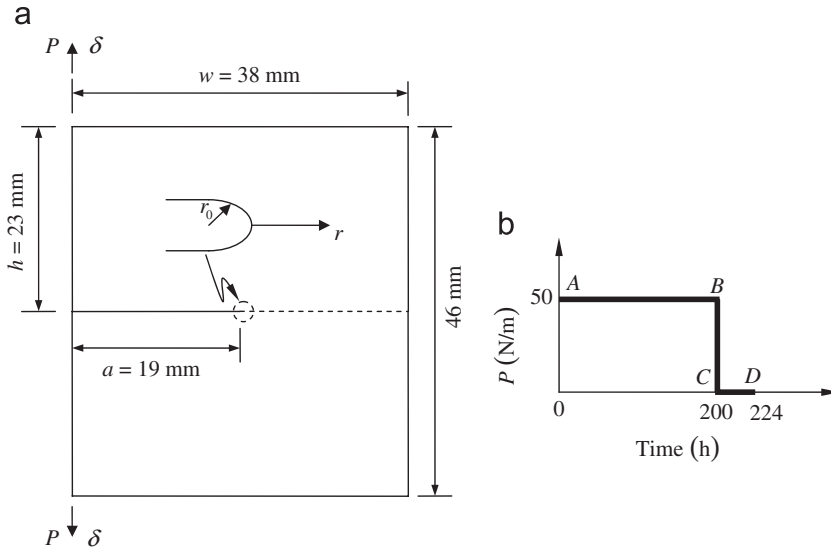


Fig. 10. (a) The compact tension specimen with notch radius 250 μm strained by an applied displacement rate $\dot{\delta}$. The reaction force in response to the point-load displacement δ is P ; (b) loading and unloading path for the “pre-load” specimen.

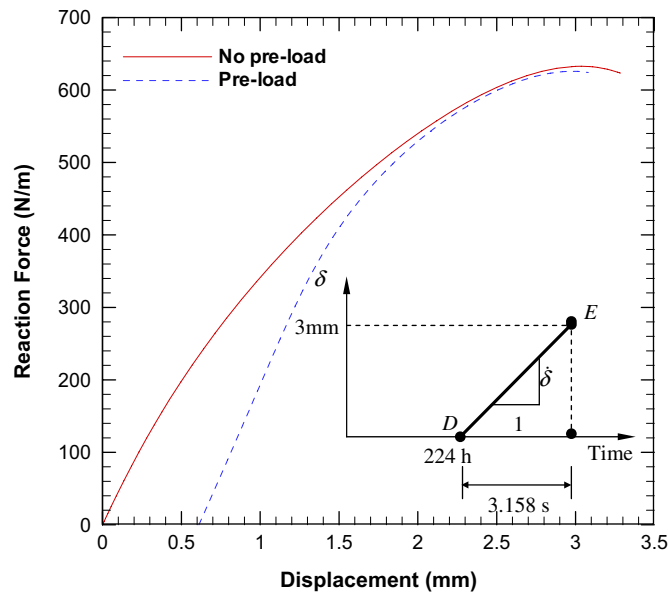


Fig. 11. Comparison of the force–displacement response between a compact tension specimen with “pre-load” and one with “no pre-load.” The inset shows the loading path by displacement for both specimens.

constitutive model, we show that pre-loading of a specimen generates microstructural damage which needs to be accounted for in any subsequent use of the specimen for fracture toughness assessment.

The geometry of the compact tension specimen is shown in Fig. 10a. The width is $w = 0.038$ m, the half-height $h = 0.023$ m, and the crack length $a = 0.019$ m. By symmetry, we analyzed only the upper half of the specimen. In the simulations, we used two specimens: one with “pre-load” and one with “no pre-load.” Before any loading, the propellant of both specimens had the same composition, the same initial constituent volume fractions, and was assumed to exhibit the same constitutive response, as has been developed in this work. Fig. 10b shows the loading path for the “pre-load” specimen: first the specimen was subjected to a constant

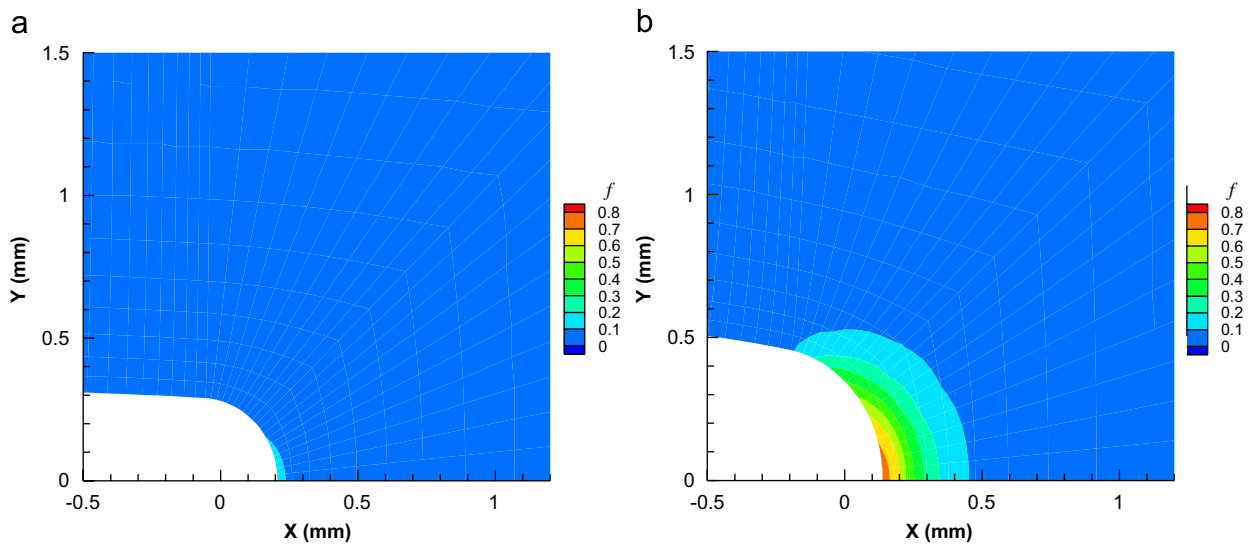


Fig. 12. Contour plots of void volume fraction around the crack-tip in the “pre-load” specimen: (a) right before re-loading (point *D* in Fig. 10b); (b) after re-loading to a displacement $\delta = 3$ mm (point *E* in Fig. 11).

force of 50.0 N/m for 200 h and then was unloaded completely and allowed to recover for 24 h before re-loading. Next, both “pre-load” and “no pre-load” specimens were loaded at a constant applied displacement rate $\dot{\delta} = 9.5 \times 10^{-4}$ m/s up to a final displacement $\delta = 0.003$ m, as shown in the inset of Fig. 11.

The macroscopic force P in response to the imposed macroscopic displacement δ is shown in Fig. 11. Clearly, the specimen with “pre-load” experiences a steeper rise of the force than the specimen with no “pre-load” as the displacement increases. The reason is that pre-loading induces damage by dewetting and this renders the material more compliant in the neighborhood of the crack tip. Fig. 12a shows the contour plot of the void volume fraction ahead of the crack tip in the specimen with “pre-load” at the end of pre-loading ($t = 224$ h). Thus, before re-loading, the “pre-load” specimen had a void volume fraction at the crack tip as large as 0.12 whereas the “no pre-load” specimen had an initial void volume fraction of 0.01 throughout. However, despite this difference in the initial damage between the two specimens, the distribution of damage in the “no pre-load” specimen tends to that with “pre-load” as the load becomes larger than about 65% of the macroscopic instability load shown by the (P, δ) curve (Fig. 11). This is demonstrated by the convergence of the two families of curves of Fig. 13 for the void volume fraction vs. distance from the crack tip. The distribution of damage ahead of the crack tip at the end of loading, $\delta = 3$ mm, which is approximately the same for both specimens is shown in Fig. 12b. The conclusion one can draw from these results is that if fracture initiates well before macroscopic instability commences, the history of loading is a parameter that needs not be overlooked in any attempt to measure the fracture toughness of the material. On the other hand, if the experimental evidence points to no crack growth before the instability point of the (P, δ) curve, the loading history of the fracture test-piece is not important. We consider the latter case very unlikely as we do not expect a crack tip embedded in an environment of void volume fraction of about 0.2 (before which pre-loading seems to matter) to remain stationary.

Pre-loading does not only induce damage in the form of porosity, but it also changes the response of the microstructure by leaving a residual back stress. Upon re-loading, this residual back stress opposes the effect of the applied stress on accumulating additional viscous strain. This diminishes the rate of change of void volume fraction up to a certain applied stress level beyond which this residual back stress effect in retarding growth relative to the “no pre-load” case ceases to be significant.

This behavior can be clearly understood in simple uniaxial tension. In this case, a “pre-load” specimen was obtained by first applying a constant axial stress $\Sigma = 0.05$ MPa for 200 h, then unloading the specimen completely, and lastly letting it recover for 24 h before testing. Both “pre-load” and “no pre-load” specimens were loaded at the same strain rate of 0.03 s $^{-1}$. Fig. 14a shows the stress and the associated evolution of the

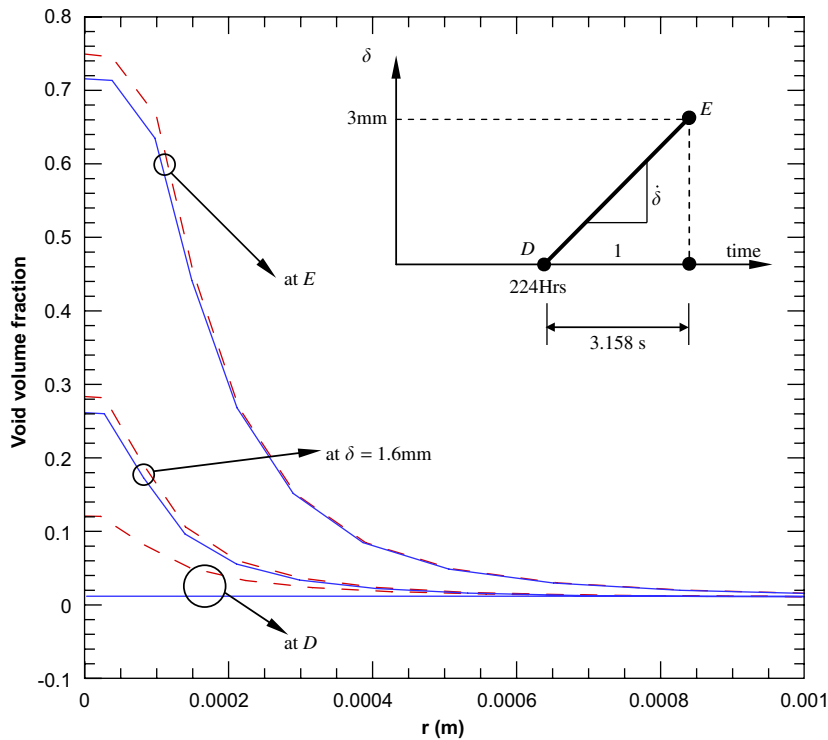


Fig. 13. Plot of the void volume fraction along the axis of symmetry ahead of the crack tip as a function of distance from the tip. The solid line is for the specimen with “no pre-load” and the dash line is for the specimen with “pre-load.”

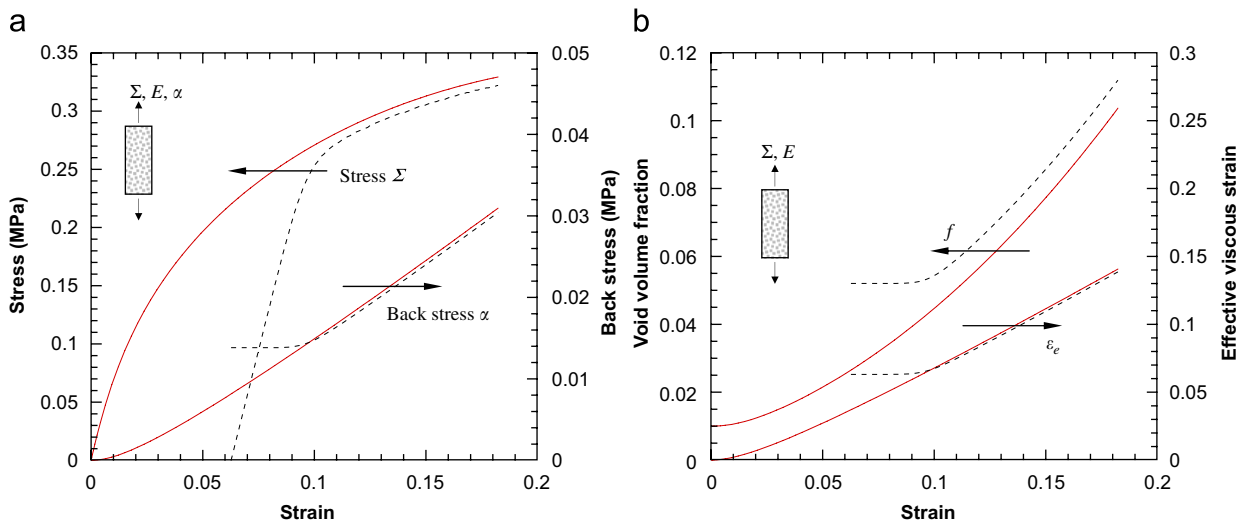


Fig. 14. Comparison of the uniaxial tension response between a specimen with “pre-load” (dash lines) and a specimen with “no pre-load” (solid lines): (a) applied stress Σ and back stress α ; (b) void volume fraction f and effective viscous strain ϵ_e .

back stress in response to an applied strain. The corresponding effective viscous strain and void volume fraction are shown in Fig. 14b. Clearly the specimen with “pre-load” has a residual back stress which causes the applied stress to differ (Fig. 14a) from that of the specimen with “no pre-load.” In fact, for strains greater than 0.1, the back stresses in the two microstructures equalize and the corresponding stresses tend to be

similar. Because of the presence of the residual back stress (Fig. 14a) in the specimen with “pre-load,” the evolution both of the void volume fraction and the effective viscous strain exhibits a plateau up to strain 0.1 (Fig. 14b). Beyond this “flat” regime, the porosities in the two specimens attain different levels, obviously in view of the different initial porosity conditions prevailing at strains smaller than 0.1, and this difference in porosity remains nearly the same as straining increases.

5. Closure

In this work, we devised a general 3-D finite-strain constitutive model for solid propellant materials by using state-of-the-art homogenization theory for nonlinear composite materials. The effect of the microstructure evolution due to particle dewetting on the constitutive response was modeled by monitoring void nucleation and growth upon straining. Matching the model predictions with experimental data from a high elongation solid propellant material required a constitutive model for the polymeric binder that was nonlinearly dependent on stress and strain; both fuel and oxidizer particles were assumed rigid in comparison to the soft polymeric binder. Such nonlinear response of the binder can be justified on the grounds of polymer chain re-orientation and rupture during straining. The model incorporates a tensorial back stress which evolves with deformation to modulate the viscous relaxation. It is noted that the model parameters can be calibrated through simple relaxation and tension experiments for the determination of (i) the constitutive response of each individual constituent phase and (ii) the critical strain statistics controlling the dewetting process.

The model was implemented in the general purpose finite element code ABAQUS through a user material routine UMAT² to simulate real-world propellant response under various loading paths. The predictions can be deemed satisfactory. The model was also implemented in the *Rocsolid* code of the Center for Simulation of Advanced Rockets at the University of Illinois to study damage evolution in the propellant grain of the Titan IV SRMU PQM-1 rocket motor.

Lastly the model was used to analyze the stress and deformation fields in a compact tension fracture specimen. The results show that the fracture response of the material can be affected by damage (measured in terms of porosity) and changes in the microstructure (measured in terms of the back stress) induced by pre-loading. The importance of this observation on the establishment of a fracture criterion for nonlinear fracture of solid propellants was discussed.

Acknowledgments

This work was supported by the Center for Simulation of Advanced Rockets, funded by the US Department of Energy through the University of California under Subcontract number DOE/LLNL/B523819. The finite element calculations were carried out at the National Center for Supercomputing Applications at the University of Illinois at Urbana-Champaign.

References

- Aravas, N., 1994. Finite-strain anisotropic plasticity and the plastic spin. *Modelling Simul. Mater. Sci. Eng.* 2, 483–504.
- Aravas, N., Ponte Castañeda, P., 2004. Numerical methods for porous metals with deformation-induced anisotropy. *Comput. Methods Appl. Mech. Eng.* 193, 3767–3805.
- Bonnenfant, D., Mazerolle, F., Suquet, P., 1998. Compaction of powders containing hard inclusions: experiments and micromechanical modeling. *Mech. Mater.* 29, 93–109.
- deBotton, G., Ponte Castañeda, P., 1993. Elastoplastic constitutive relations for fiber-reinforced solids. *Int. J. Solids Struct.* 30, 1865–1890.
- Canga, M.E., Becker, W.B., Özüpek, S., 2001. Constitutive modeling of viscoelastic materials with damage-computational aspects. *Comput. Methods Appl. Mech. Eng.* 190, 2207–2226.
- Cheng, C., Aravas, N., 1997. Creep of metal–matrix composites with elastic fibers—part I: continuous aligned fibers. *Int. J. Solids Struct.* 34, 4147–4171.
- Chu, C.C., Needleman, A., 1980. Void nucleation effects in biaxially stretched sheets. *J. Eng. Mater. Technol.* 102, 249–256.

²Copies of the computer code (UMAT) will be supplied upon request. Please address inquiries to Prof. Sofronis at the e-mail address sofronis@uiuc.edu.

- Cornwell, L.R., Schapery, R.A., 1975. SEM study of microcracking in strained solid propellant. *Metallography* 8, 445–452.
- Dafalias, Y.F., 1987. Issues on the constitutive formulation at large elastoplastic deformations, part 1: kinematics. *Acta Mech.* 69, 119–138.
- Dafalias, Y.F., 1988. Issues on the constitutive formulation at large elastoplastic deformations, part 2: kinetics. *Acta Mech.* 73, 121–146.
- Dafalias, Y.F., 1990. The plastic spin in viscoplasticity. *Int. J. Solids Struct.* 26, 149–163.
- Dafalias, Y.F., 1998. Plastic spin: necessity or redundancy? *Int. J. Plasticity* 14, 909–931.
- Dienes, J.K., Zuo, Q.H., Kershner, J.D., 2006. Impact initiation of explosives and propellants via statistical crack mechanics. *J. Mech. Phys. Solids* 54, 1237–1275.
- Farber, J.N., Farris, R.J., 1987. Model for prediction of the elastic response of reinforced materials over wide ranges of concentration. *J. Appl. Pol. Sci.* 34, 2093–2104.
- Farris, R.J., 1968. The influence of vacuole formation on the response and failure of filled elastomers. *Trans. Soc. Rheol.* 12, 315–334.
- Francis, E.C., Thompson, R.E., 1984. Nonlinear structural modeling of solid propellants. In: *Proceedings of the AIAA/SAE/ASME joint Propulsion Conference*. AIAA, New York, pp. 1–5.
- Ganzonas, G., 1993. A uniaxial nonlinear viscoelastic constitutive model with damage for M30 gun propellant. *Mech. Mater.* 15, 323–335.
- Ha, K., Schapery, R.A., 1998. Three-dimensional viscoelastic constitutive model for particulate composites with growing damage and its experimental validation. *Int. J. Solids Struct.* 35, 3497–3517.
- Hashin, Z., Shtrikman, S., 1963. A variational approach to the theory of the elastic behavior of multiphase materials. *J. Mech. Phys. Solids* 11, 127–140.
- Hibbitt, H.D., 1977. ABAQUS/EPGEN—a general purpose finite element code with emphasis in nonlinear problems. *Nucl. Eng.* 7, 271–297.
- Hinterhoelzl, R.M., Shapery, R.A., 2004. FEM implementation of a three-dimensional viscoelastic constitutive model for particulate composites with damage growth. *Mech. Time-Dependent. Mater.* 8, 65–94.
- Ho, S.-Y., 2002. High strain-rate constitutive models for solid rocket propellants. *J. Prop. Power* 18, 1106–1111.
- Jung, G.-D., Youn, S.-K., 1999. A nonlinear viscoelastic constitutive model of solid propellant. *Int. J. Solids Struct.* 36, 3755–3777.
- Jung, G.-D., Youn, S.-K., Kim, B.-K., 2000. A three-dimensional nonlinear viscoelastic constitutive model of solid propellant. *Int. J. Solids Struct.* 37, 4715–4732.
- Kailasam, M., Aravas, N., Ponte Castañeda, P., 2000. Porous metals with developing anisotropy: constitutive models, computational issues and applications to deformation processing. *Comput. Model. Eng. Sci.* 1, 105–118.
- Lee, E.H., Mallett, R.L., Wertheimer, T.B., 1983. Stress analysis for anisotropic hardening in finite-deformation plasticity. *J. Appl. Mech.* 50, 554–560.
- Little, R.R., Rice, J.R., 2004. Further studies in solid propellant fracture toughness testing. In: *Proceedings of the JANNAF 36th Structures and Mechanical Behavior Subcommittee Meeting*, CD-ROM, New Orleans, LA.
- Matheson, E.R., Nguyen, D.Q., 2005. A rate-dependent viscoelastic damage model for simulation of solid propellant impacts. In: *Furnish, Elert, Rusell, White (Eds.), Shock Compression of Condensed Matter*. American Institute of Physics, pp. 913–916.
- Matouš, K., Geubelle, P.H., 2006. Multiscale modeling of particle debonding in reinforced elastomers subjected to finite deformation. *Int. J. Numer. Mech. Eng.* 65, 190–223.
- McLean, M., 1985. Creep deformation of metal–matrix composites. *Compos. Sci. Technol.* 23, 37–52.
- Mori, T., Tanaka, K., 1973. Average stress in matrix and average elastic energy of materials with misfitting inclusions. *Acta Metall.* 21, 571–574.
- Needleman, A., 1985. On finite element formulations for large elastic–plastic deformations. *Comput. Struct.* 20, 247–257.
- Özüpek, S., Becker, E.B., 1992. Constitutive modeling of high-elongation solid propellants. *J. Eng. Mater. Technol.* 114, 111–115.
- Özüpek, S., Becker, E.B., 1997. Constitutive equations for solid propellants. *J. Eng. Mater. Technol.* 119, 125–132.
- Park, S.W., Schapery, R.A., 1997. A viscoelastic constitutive model for particulate composites with growing damage. *Int. J. Solids Struct.* 34, 931–947.
- Ponte Castañeda, P., 1991. The effective mechanical properties of nonlinear isotropic solids. *J. Mech. Phys. Solids* 39, 45–71.
- Ponte Castañeda, P., 1992. New variational principles in plasticity and their application to composite materials. *J. Mech. Phys. Solids* 40, 1757–1788.
- Ponte Castañeda, P., 1996. Exact second-order estimates for the effective mechanical properties of nonlinear composites materials. *J. Mech. Phys. Solids* 44, 827–862.
- Ponte Castañeda, P., Suquet, P., 1998. Nonlinear composites. *Adv. Appl. Mech.* 34, 171–302.
- Ravichandran, G., Liu, C.T., 1995. Modeling constitutive behavior of particulate composites undergoing damage. *Int. J. Solids Struct.* 32, 979–990.
- Rice, J.R., 1970. On the structure of stress–strain relations for time-dependent plastic deformation in metals. *J. Appl. Mech.* 37, 728–737.
- Schapery, R.A., 1981. On viscoelastic deformation and failure behavior of composite materials with distributed flaws. In: *Wang, S.S., Renton, W.L. (Eds.), 1981 Advances in Aerospace Structures and Materials*. ASME, AD-01, New York, pp. 5–20.
- Schapery, R.A., 1989. Models for the deformation of viscoelastic media with distributed damage and their applicability to ice. In: *Proceedings of the IUTAM/IAJR Symposium on Ice/Structure Interaction*, Memorial University of Newfoundland, St John's.
- Schapery, R.A., 1990. Theory of mechanical behavior of elastic media with growing damage and other changes in structure. *J. Mech. Phys. Solids* 38, 215–253.
- Schapery, R.A., 1991. Analysis of damage growth in particulate composites using a work potential. *Compos. Eng.* 1, 167–182.
- Simo, J.C., 1987. On a fully three-dimensional finite-strain viscoelastic damage model: formulation and computational aspects. *Comput. Methods Appl. Mech. Eng.* 60, 153–173.

- Suquet, P., 1985. Elements of homogenization for inelastic solid mechanics. In: Sanchez-Palencia, Zaoui, A. (Eds.), *Lecture Notes in Physics*, No 272, Homogenization Techniques for Composite Media. Springer-Verlag, New York, pp. 193–278.
- Suquet, P., 1995. Overall properties of nonlinear composites: a modified secant moduli theory and its link with Ponte Castañeda's nonlinear variational procedure. *C.R. Acad. Sci. Paris II b* 320, 563–571.
- Suquet, P., 1996a. Overall properties of nonlinear composites: remarks on secant and incremental formulations. In: Pineau, A., Zaoui, A. (Eds.), *Micromechanics of Plasticity and Damage of Multiphase Materials (IUTAM Symposium)*. Kluwer, Dordrecht, The Netherlands, pp. 149–156.
- Suquet, P., 1996b. Overall properties of nonlinear composites: secant moduli theories and variational bounds. In: Markov, K.Z. (Ed.), *Continuum Models of Discrete Systems (CMDS8 Symposium)*. World Scientific, Singapore, pp. 290–299.
- Suquet, P., 1997. Effective properties of nonlinear composites. In: Suquet, P. (Ed.), *Continuum Micromechanics*, ICMS No. 377. Springer, Wien, New York, pp. 197–264.
- Sutton, G.P., 1986. *Rocket Propulsion Elements*. Wiley, New York.
- Swanson, S.R., Christensen, L.W., 1983. A constitutive formulation for high-elongation propellants. *J. Spacecrafts Rockets* 20, 559–566.
- Tan, H., Liu, C., Huang, Y., Geubelle, P.H., 2005a. The cohesive law for the particle/matrix interfaces in high explosives. *J. Mech. Phys. Solids* 53, 1892–1917.
- Tan, H., Huang, Y., Liu, C., Geubelle, P.H., 2005b. The Mori–Tanaka method for composite materials with nonlinear interface debonding. *Int. J. Plasticity* 21, 1890–1918.
- Tan, H., Huang, Y., Liu, C., Ravichandran, G., Inglis, H.M., Geubelle, P.H., 2007. The uniaxial tension of particulate composite materials with nonlinear interface debonding. *Int. J. Solids Struct.* 44, 1809–1822.
- Trumel, H., Dragon, A., Fanget, A., 1996. A finite-strain elastic–plastic model for the quasi-static behavior of particulate composites. *Int. J. Eng. Sci.* 34, 677–698.
- Trumel, H., Dragon, A., Fanget, A., Lambert, P., 2001a. A constitutive model for the dynamic and high strain-pressure behavior of a propellant-like material: Part I: experimental background and general structure of the model. *Int. J. Numer. Anal. Methods Geomech.* 25, 551–579.
- Trumel, H., Dragon, A., Fanget, A., Lambert, P., 2001b. A constitutive model for the dynamic and high strain-pressure behavior of a propellant-like material: Part II: model development and applications. *Int. J. Numer. Anal. Methods Geomech.* 25, 581–603.
- Vratsanos, L.A., Farris, R.J., 1993a. A predictive model for the mechanical behavior of particulate composites, Part I: model derivation. *Pol. Eng. Sci.* 33, 1458–1465.
- Vratsanos, L.A., Farris, R.J., 1993b. A predictive model for the mechanical behavior of particulate composites, Part II: comparison of model predictions to literature data. *Pol. Eng. Sci.* 33, 1466–1474.
- Xu, F., 2008. *Micromechanics approach to the study of constitutive response and fracture of solid propellant materials*. Ph.D. Thesis, University of Illinois at Urbana-Champaign, 2008.
- Xu, F., Sofronis, P., Aravas, N., Meyer, S., 2007. Constitutive modeling of porous viscoelastic materials. *Eur. J. Mech./A Solids* 26, 936–955.